Effect of Devitrification Temperature on the Microstructure of NiTi Films

by

Michael Joseph Vestel

B.S. (Alfred University) 1992

M.A. (University of California, Los Angeles) 1997

A dissertation submitted in partial satisfaction of the

requirements for the degree of

Doctor of Philosophy

in

Engineering-Materials Science and Engineering

in the

GRADUATE DIVISION

of the

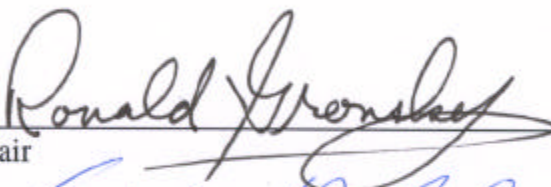UNIVERSITY OF CALIFORNIA, BERKELEY

Committee in charge:

Professor Ronald Gronsky
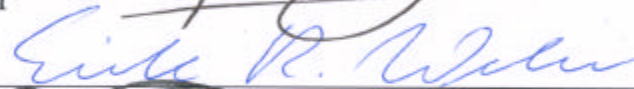
Professor Albert P. Pisano

Professor Eicke Weber

Spring 2002

The dissertation of Michael Joseph Vestel is approved:

_____   05/20/02
Chair   Date

_____   May 20, 2002
                                                                    Date

_____   21 MAY 2002
                                                                    Date

University of California, Berkeley

Spring 2002

Effect of Devitrification Temperature on the Microstructure of NiTi Films

Copyright (2002)

Michael Joseph Vestel

Abstract

Effect of Devitrification Temperature on the Microstructure of NiTi Films

by

Michael Joseph Vestel

Doctor of Philosophy in Engineering-Materials Science and Engineering

University of California, Berkeley

Professor Ronald Gronsky, Chair

Crystalline nickel titanium (NiTi) films are known to possess superelastic properties offering superior advantages in engineering applications where resilient mechanical response is essential. One such application of increasing importance in the biomedical field is the fabrication of micro-needles for transdermal or subdermal fluid transport, including the integration of micro-needles with silicon structures such as bio-MEMS assemblies. Unfortunately, the direct deposition of Ni-Ti alloys onto silicon is sometimes compromised by grossly mismatched thermal expansion coefficients resulting in delamination and spalling of the metallic films. This obstacle can be overcome by depositing the metallic alloy as an amorphous phase followed by a release of the amorphous film, and then a crystallization anneal (also called "devitrification" since it

1

follows from a glassy phase) to develop the microstructure needed to induce the superelastic effect.

This work seeks to understand the effect of devitrification temperature on the microstructure of crystallized, freestanding amorphous NiTi films and the kinetics of the crystallization transformation. This has been accomplished using transmission electron microscopy (TEM) combined with differential scanning calorimetry (DSC) and x-ray energy dispersive spectrometry (EDS). Results reported here indicate that the free surface of the film transforms differently and results in a different microstructure than the interior of the film. The grains that nucleate at the surface grow into the film in a columnar fashion and transform mostly between the rhombohedral phase and the austenite phase when thermally cycled between –100ºC and 200ºC. The interior of the film crystallizes separately from the columnar grains to form platelets. These platelet grains transform between martensite and austenite when thermally cycled between -100ºC and 200ºC.

Temperatures as low as 390ºC are reported here to partially crystallize amorphous films removed from a substrate, while crystallizing at 400ºC is shown to fully crystallize the amorphous film. The film crystallized at 420ºC for 200 minutes was fully characterized with TEM, electrons energy loss spectroscopy (EELS), EDS and DSC, showing CMOS compatible temperatures can be used to produce fully crystalline NiTi films that undergo phase transformations between martensite, austenite and an intermediate rhombohedral phase.

Dedication

I wish to dedicate this dissertation to my wife, Leora Broydo. Her continued support of my endeavors, from building redwood hot tubs to pursuing my Ph. D., from building nano-breweries to working on my Masters, has been unending. Her love is unconditional, her inspiration moving and her friendship steadfast. Without her I would be lost.

I also wish to dedicate this dissertation to my parents, William and Carolynn Vestel. They always believed I could do what I set my mind to. Thank you.

Finally, a heart felt thank you to my extended family, Lina and Sam Broydo. I wish to offer Sam special thanks for his technical advice in every aspect of my career. He has been incredible to work with, but his support has also been in his inspiring anecdotes. And to Lina, who has always been there when Leora and I have needed a word to pick us up or a little get away to rejuvenate. Thank you for being such a great mother to my wife and treating me like a son.

Table of contents

List of Figures

Acknowledgments

1   Introduction

The shape memory effect (SME) and super-elastic effect (SE) involve a thermally induced or mechanically (figure 1) induced solid-state, crystalline phase transformation between a ductile martensitic phase and a stiffer austenitic phase (M-A transformation). The terminology of a low temperature martensite phase and high temperature austenite phase are borrowed from the naming of the high temperature and low temperature phases of steel alloys. Superelasticity is the ability for a material to elastically absorb large strains (3-10%) due to this reversible phase transformation. The SME refers to the ability of a material to be deformed in its low temperature phase, martensite, and then transform or remember its original shape when heated to its high temperature phase, austenite.

The shape memory effect and super-elastic effect are exhibited by a number of shape memory alloys (SMAs) including In-Tl, Cu-Zn and Cu-Al-Ni. The first SMA, Au-47.5 at% Cd, was
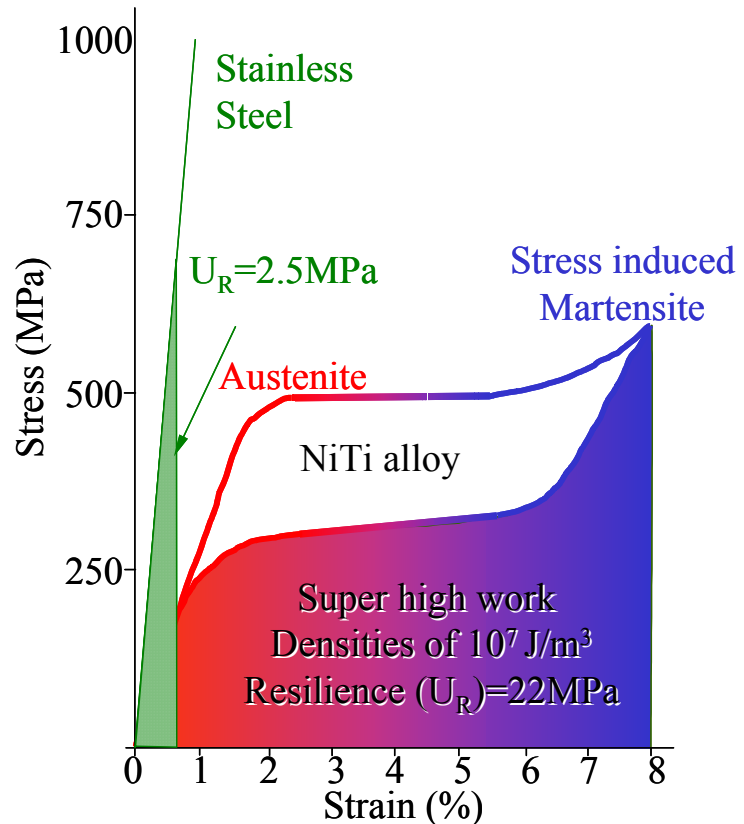
Figure 1: Resilience of stainless steel and NiTi compared (shaded area). The large strains and large recoverable stresses associated with the solid-state phase transformation lead to exceptionally high energy densities, which can be exploited in MEMS actuators and sensors and damping components.

discovered in 1951 [1] but the most technologically important SMA, Ni-Ti, was discovered in 1963. Nickel titanium has since been used in bulk form to make pipe couplings, antennas for cell phones, medical implants and guide-wires, and various actuators in electric appliances [1]. In addition, temperature sensitive switches and robotic manipulators have been fabricated from the bulk [2].

Crystalline NiTi films are also known to possess superelastic properties [1, 3-9] and display a shape memory effect, offering superior advantages in engineering applications where resilient mechanical response is essential or where thermal actuation is desired, including MicroElectroMechanical systems (MEMS). One such application of increasing importance in the biomedical field is the fabrication of micro-needles [10-19] for transdermal or subdermal fluid transport, including the integration of micro-needles with silicon structures [20] such as bio-MEMS assemblies. Unfortunately, the direct deposition of Ni-Ti alloys onto silicon is sometimes compromised by grossly mismatched thermal expansion coefficients [21, 22] resulting in delamination and spalling of the metallic films. This obstacle can be overcome by depositing the metallic alloy as an amorphous phase [1, 3-9] followed by a release of the amorphous film, and then a crystallization anneal (also called "devitrification" since it follows from a glassy phase) to develop the microstructure needed to induce the superelastic effect [1, 3-8].

Because actuation of a NiTi MEMS device is done thermally, NiTi films can function both as actuator and thermal sensor.

Nickel titanium films have received considerable attention for applications in micro and millimeter scale applications [23-29] since NiTi was first integrated with a

micro-machining process by Walker *et. al.*, in 1989 [30, 31]. The reasons for the recent

surge in interest among the MEMS community are numerous. NiTi has an energy density

10-100 times greater than other MEMS actuators due to a solid-state phase

transformation. Its biocompatibility surpasses that of stainless steel. Its fatigue resistance

allows NiTi films to be strained thousands of times by 3% when stressed around 350

MPa. Such high actuation forces and high recoverable strains offer significant advantages

compared to other actuator materials like silicon which can only be strained by 0.2%

repeatedly. It can be heated resistively with low driving voltages and has a high switching

rate in the 1 to 100Hz range due to the rapid heat transfer associated with the film form

[23, 31, 32]. Furthermore, the sputtered form has led to the SMA being batch fabricated

and thus has potential for integration with control electronics [30-32].

Another unique aspect of NiTi SMA is its high damping capacity [34-52]. Most

viscoelastic materials do not combine
such high strength together with high
damping as does NiTi [36]. The high
damping can occur when martensite is
thermally or mechanically induced. The
extraordinary damping effect is due to the
energy going into the phase
transformation. In addition, the intrinsic
damping of martensite is very high. This
is because the martensite twin variants
reorient under applied stress [36].
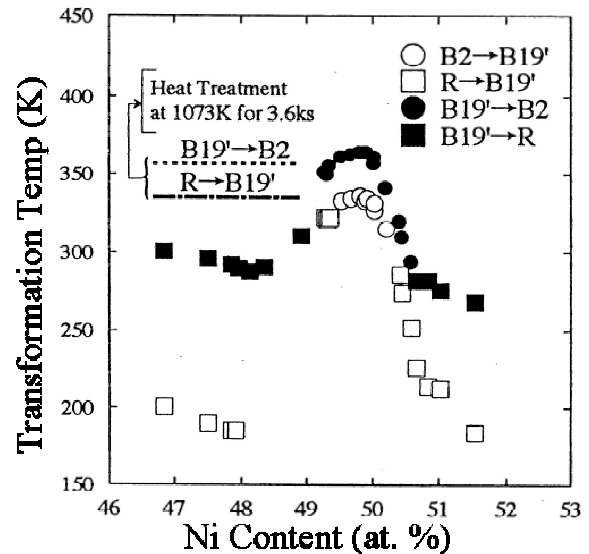
Figure 2: Variation of phase transformation temperatures as a function of Ni content for nearly equiatomic Ni-Ti sputtered films [33]. These films were crystallized from the amorphous state at 500°C-800°C for 1 hour.

3

The ability for the phase transformation temperatures that are responsible for the SME and SE to be tuned to a desired temperature is presented in figure 2 [33]. The phase transformation temperatures for near equiatomic NiTi alloys increases from −73°C to 77°C with a decrease of only 1½ at. % Nickel.

Films of NiTi are typically processed one of two ways. They are either sputter deposited above 430°C, in which case the films are crystalline [4], or they are sputter deposited below 430°C and the resulting films are amorphous. The amorphous films are usually crystallized at temperatures higher than the measured dynamic crystallization temperature, T_x [7, 9, 54, 55]. The dynamic crystallization temperature is usually measured via differential scanning calorimetry (DSC) and is defined as the onset of the exothermic peak, which results from crystallization. An example of a DSC curve used to determine a film's dynamic crystallization temperature is presented in figure 3.

Deposition of NiTi in the amorphous state [1, 3-9] allows thick (>5-7μm) films to be deposited onto silicon, solving delamination and spalling problems associated with grossly mismatched thermal expansion coefficients between the alloy film and the substrate. The amorphous film
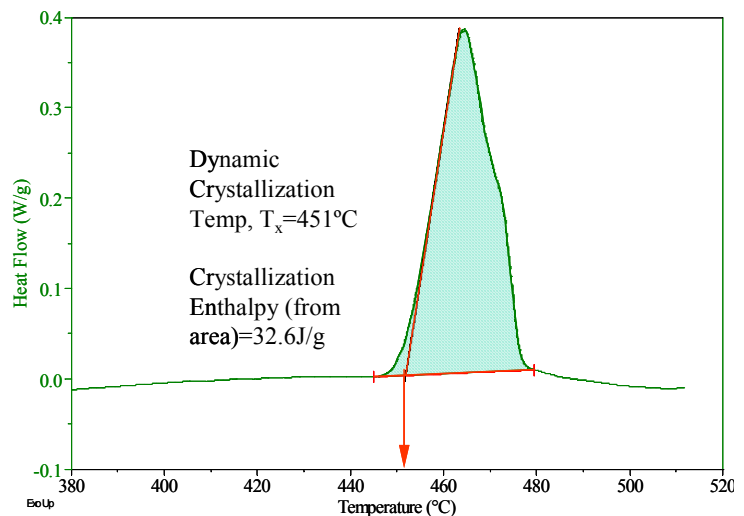
Figure 3: Isochronal DSC measurement (10K/min) of 22μm amorphous equiatomic NiTi film released from a stainless steel substrate (film 1) showing the dynamic crystallization temperature to be ~450°C. The crystallization liberated 32.6J/g of energy. Both of these values compare well with published values [53]. This crystallization temperature represents the upper limit for crystallization experiments done in the present work.

4

can then be removed from the substrate (to avoid the same problems associated with thermal expansion mismatch) and crystallized.

Most work has been done at temperatures above T_x, but no systematic study has been done on the effect of annealing amorphous NiTi films below this temperature. Such low temperature, post processing crystallization anneals would be favorable for their CMOS compatibility. The work presented here addresses the microstructural development of freestanding amorphous NiTi alloys when heated below T_x, between 380ºC and 450ºC.

2   Background

2.1   Super-elastic Effect

When the shape memory alloy is fully austenitic, a stress will assist the martensitic transformation, figure 4. Superelasticity is the ability of a material to elastically absorb large strains (3-10%) due to this stress induced, reversible phase transformation. If the stress applied does not cause dislocation assisted slip the
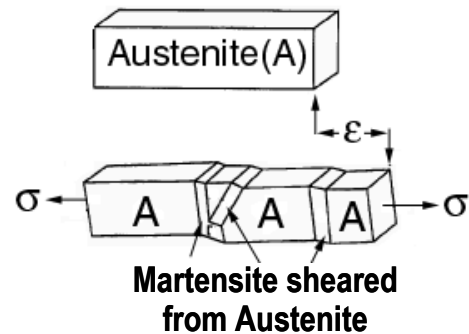
Figure 4: Austenite deformed into martensite when a SE alloy is stressed.

material will revert back to austenite, recovering the pre-deformed shape. This is because when the stress is released the martensite is thermodynamically unstable and will revert back to the parent austenitic phase. When stressed, the austenite transforms to martensite. Multiple martensite variants separated by twin boundaries will form from each austenite grain. Martensite variants aligned properly with the applied stress will grow at the

expense of the other martensite variants through motion of twin boundaries. The multiple

martensite variants formed will revert back to the original austenitic crystal structure in

the original crystallographic orientation, hence the strain becomes reversed upon

unloading
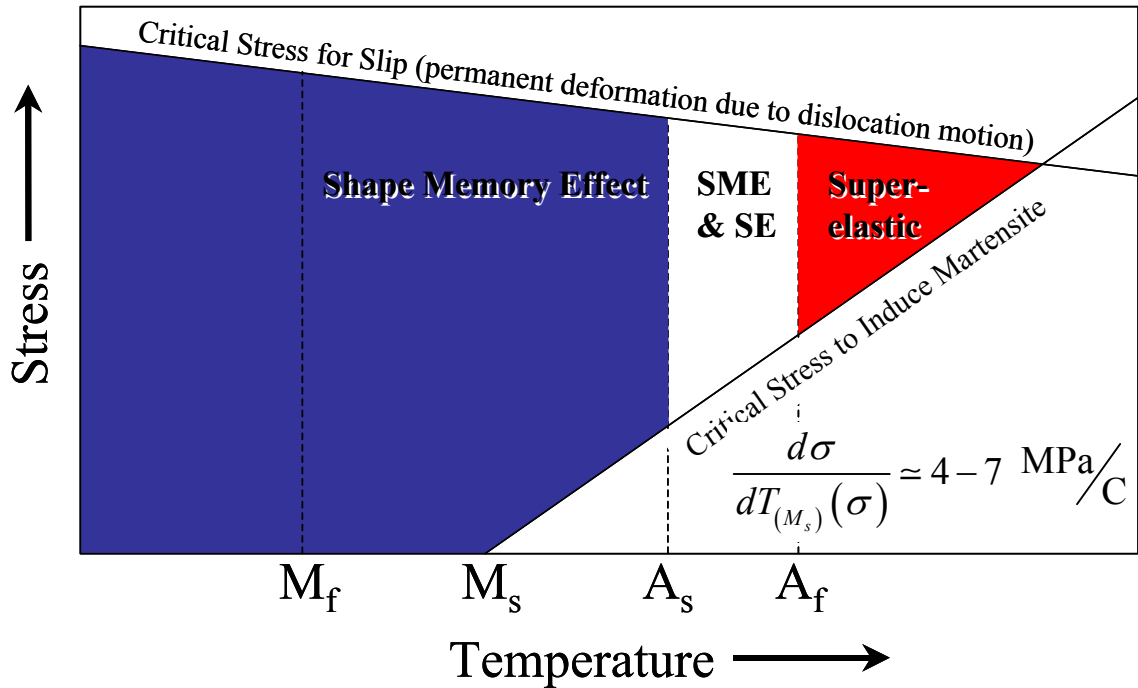
Figure 5: Schematic diagram showing the how stress and temperature determine when the shape memory effect & the super-elastic effect are observed.

The super-elastic effect and the shape memory effect are both due to the

crystallographic reversibility of the martensite-austenite (M-A) transformation, without

the formation of irreversible dislocations formed during slip. Both effects can be

observed in the same specimen depending on the test temperature, as illustrated in figure

5, following Otsuka [1(p.41)]. The shape memory effect is observed when tested below

the austenitic start temperature, A_s. When stressed above A_f, the austenitic finish

temperature, the alloy will behave in a superelastic fashion. Between A_s and A_f, both

effects partially occur. The straight line with a positive slope represents how the stress

required to induce martensite (stress induced martensite) changes with temperature. This relationship is described by the Clausius-Clapeyron relationship and is derived in Appendix with a sample calculation for Ni-Ti. The important result is the stress at which martensite will form changes with temperature according to the Clausius-Clapeyron relationship:

$$\frac{d\sigma}{dT_0(\sigma)} = \frac{-1}{V_0 \bullet T_0(0)} \frac{(\Delta H_{A \to M})}{(\Delta \varepsilon_{A \to M})}$$

Because the enthalpy $\Delta H_{A \to M}$ of the austenite to martensite transformation is negative (it gives off heat and is thus exothermic) and the strain $\Delta \varepsilon_{A \to M}$ associated with this transformation is positive, the slope will be positive as shown in figure 5. For NiTi, the slope will be around 4-7MPa per degree K or C[56].

Figure 6: Schematic of the Shape Memory Effect [24].

The stress-strain relationship of a superelastic alloy is shown in figure 1, showing that the energy density stored as a result of the phase transformation is 10-100 times greater than other materials. Also illustrated in this figure is how the stress induces the martensite at a constant stress and how very large strains are fully recoverable.

2.2   The Shape Memory Effect

A schematic of the SME is shown in figure 6. When cooled to the low temperature martensitic phase, the NiTi microstructure forms self-accommodating

martensite twins and is easily deformed. Deformation of the martensite occurs by a selective migration of twin boundaries in the multi-variant grain structures. That is, certain twin variants aligned properly with the applied stress grow at the expense of others martensite variants. When heated, each martensite variant (including those that shrank during deformation) reverts back to the parent austenitic phase in the original orientation by the reverse transformation. Upon this phase transformation, the material recovers its original shape.
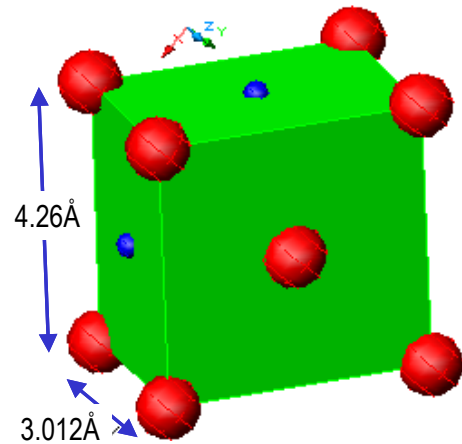
Figure 7: The NiTi, B2, Austenitic crystal structure. It can also be drawn as a perfect cube with one atom on the corners and one at half the body diagonal.

2.3   Crystallography of Transformations

Anytime twin boundary motion occurs, atoms move halves of angstroms at the speed of sound and a huge amount of heat is obviously generated. Twin boundary motion occurs when the parent austenite transforms to stress-induced martensite in super-elastic alloys, diagrammatically shown in figure 4. Twin boundaries also move in shape memory alloys when martensite variants properly oriented with the applied stress consume unfavorably oriented ones. These are called
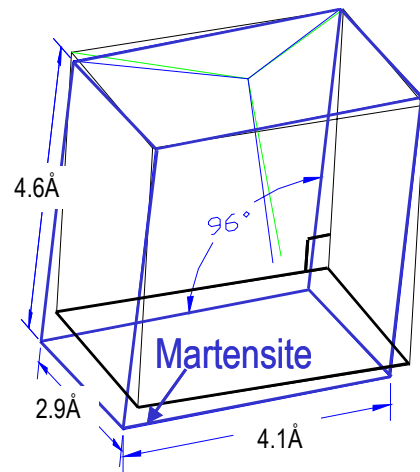
Figure 8: A-M transformation. The box translates to the new position when martensite (B19') is formed. These are accurately drawn for NiTi, and the largest atom motion shown here is on the order of half an angstrom.

8

military or diffusionless transformations because atoms move less than inter-atomic spacing but move collectively with an audible "crack". Enough heat is generated that it could almost burn your lip, if one were to bend an austenitic SE wire or deform a SMA spring on one's lip. During the A-M phase transformation, the atoms are displace from the B2 crystal structure to the B19' crystal structure. The B2 crystal structure is shown in figure 7. The amount the atoms are displaced during the transformation can be seen by observing how much the corners of the box move, figure 8. This is the same box shown in figure 7 without the atoms drawn in. The internal friction from the atom motion leads to dissipated energy (heat) and to the hysteretic loop losses in the stress-strain curve (non-shaded portion of figure 1), and is responsible for the superior damping properties of NiTi [36].

During the A-M transformation, there are 24 variants of martensite that can form from a single austenite grain. Only one of the 24 ways the deformed box can be drawn is shown in figure 8, but it is easy to see that if a different shear stress were applied, a different variant would be formed. What makes SMAs unique is that during the reverse transformation, accomplished by adding heat (SMA) or releasing the stress (SE), the atoms can only snap back to their original simple cubic austenitic crystal structure. When doing so, the original macroscopic shape is recovered.

2.4   Strategy for NiTi Actuators

MEMS based actuators require a bias force to counter the actuator force provided by the shape memory effect of the NiTi film. The bias force is used to deform the actuator when the NiTi SMA is cooled to its more ductile, compliant state. The bias force must cause the martensite to deform past its elastic limit of about 0.5% and cause twin

boundary glide to occur. To maximize the useful work but allow many cycles, the actuator should be deflected to the strain limit, about 3%. Past this, dislocation plasticity may occur, reducing the thermo-mechanical cycle lifetime[23, 24, 57].

3   Previous Work

3.1   Grain Size Refinement

When slip occurs by dislocation motion, the resulting strain is not recoverable. If SIM is reached before austenite slips, superelastic behavior will be achieved. Increasing the strength of austenite increases the resistance to slip thus yielding a larger recoverable strain.

Grain size refinement increases austenitic strength resulting in a large magnitude of recoverable strain (enhanced super-elasticity) in NiTi films [1(p. 65), 4-9, 58, 59]. The desire to control grain size and therefore improve super-elasticity was a motivation of the present study. The temperature at which the film was crystallized was thought to have some impact on the grain size. A systematic study of the effect devitrification temperature has on grain size in NiTi films, however, has yet to be done. Nor has there been a systematic study of low temperature devitrification of NiTi films, an area of importance for CMOS compatible MEMS processes.

3.2   Crystallization Temperatures

Most researchers have crystallized amorphous NiTi films using temperatures near and above the dynamic crystallization temperature (~480ºC for a 10ºC/min isochronal anneal) [28-30, 58-66]. These researchers report grain sizes between half and a few microns. No work this researcher is aware of, however, has been done at low

temperatures, though there is one report of annealing at 420ºC for 1 hour yielding grains of approximately one micron [67]. It is expected that large undercoolings should provide the driving force for producing more nuclei (smaller grains). It is clear that lower temperatures should yield devitrification, though the time to do so will increase.

3.3   Transformation Kinetics

Classical nucleation kinetics have been used to successfully describe devitrification in amorphous alloys [68, 69, 70(p.160 & 145)], because the nucleation and growth process can be identical to that in liquids. Amorphous alloys offer a unique opportunity to test classical theories at large undercoolings [70(p.146)]. Crystallization has been observed to occur by nucleation and growth for metallic glasses [68, 70] and NiTi [22, 71, 72] and it is thus expected that classical nucleation theory will accurately describe the low temperature devitrification process for amorphous, freestanding NiTi films.

The largest possible undercooling (ΔT) is desirable for the formation of small grains required to avoid dislocation slip before the formation of SIM. On the other hand, undercooling limits diffusion and nucleation rate and thus has an upper limit.

If the amorphous NiTi phase is cooled below a critical temperature, there is a driving force for the nucleation of the austenitic phase. This driving force is proportional to the undercooling. Undercooling is the difference between the critical temperature (T_m) and the lower temperature at which crystallization is done. The formation of crystalline nuclei, however, is mitigated by the fact that a free surface is created between the

11

amorphous phase and the crystalline phase when a small embryo is formed. This embryo will shrink in size and disappear if it does not have enough energy to reach a critical size.

The activation energy required to produce a critical-sized nucleus, ΔG^*, is a linear combination of a barrier term from the surface energy plus a temperature dependent driving force term. It has been shown that ΔG^* is proportional to $1/(\Delta T)^2$, so large undercoolings reduce the activation energy significantly. The number of nuclei formed as well as the nucleation rate are related to the magnitude of the critical activation energy ΔG^* and thus the undercooling. Larger undercooling (small ΔG^*) yields reduced grain size and more nuclei but slower nucleation rates.

The slower nucleation rate is a result of slower diffusion of atoms to the embryos/amorphous interface. For the NiTi polymorphic crystallization, there is a topological reconstruction of the atomic arrangement and the distance for motion is on the order of interatomic spacing. Therefore there is a limit to how large an undercooling can be used for the nucleation to occur in a practical amount of time. One of the main goals is to determine how large of an undercooling is practical.

3.4   Phase Identification via Diffraction Patterns

It is well documented that by rotating to a [111] zone axis of the B2 structure (austenite), the phase identification of a grain contained within the intermediate aperture can be identified as either B2 (austenite), R-phase, or B19' (martensite) by simply looking for the presence of extra (super) reflections as shown in figure 9 and figure 10 [1(p.57), 3, 4, 6, 73, 74]. If only the major $\langle \bar{1}10 \rangle$ spots appear, the phase is the high temperature austenitic (B2) phase. If minor (super-lattice) spots appear at 1/2 the major

$\langle \overline{1}10 \rangle$ spots, the phase is the low temperature, martensitic (B19'), while if minor spots

appear at 1/3 the major $\langle \overline{1}10 \rangle$ spots, the phase is the intermediate temperature

rhombohedral (R) phase. Note that for the B2 and R-phases, the major reflections are

indexed differently than $\langle \overline{1}10 \rangle$, as shown in figure 9 and figure 10.

Martensite Zone=[1 0 1]

● Fundamental
○ Superlattice
× Forbidden
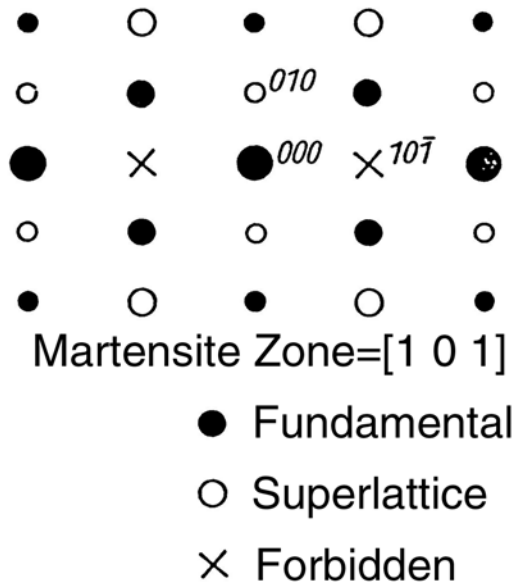
Figure 9: Schematic diffraction pattern. Spots occur at ½ the [020] B19' reflections when martensite is present. Note that only one set of spots occur at the ½ position for each variant present. If "forbidden" reflections occur, than more than one variant is captured within the intermediate aperture.
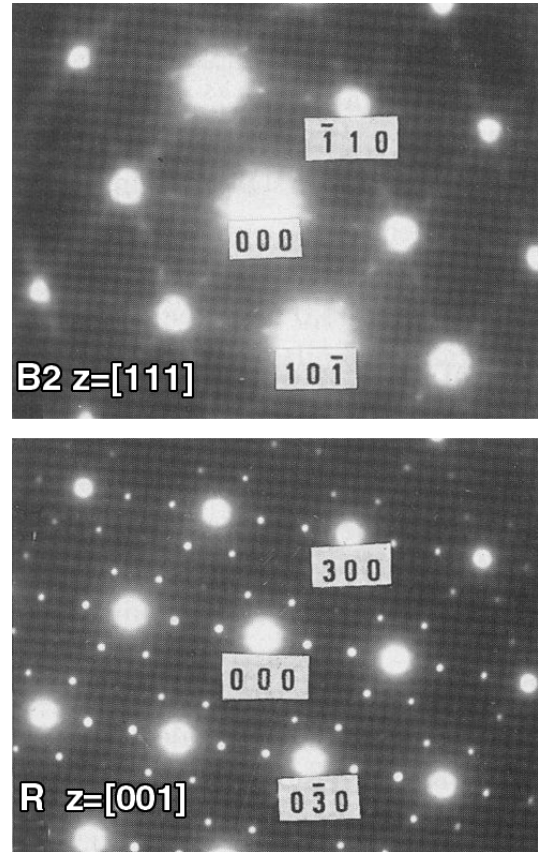
Figure 10: Experimental diffraction patterns from the B2 (austenite) phase in the [111] zone showing only major [7] reflections, and the R-phase showing 1/3 [9] spots. By simply rotating to the [111] zone of the parent phase (which is evident in all three phases), phase identification is simply done by looking for extra reflections.

4 Procedure

Nearly equiatomic films were deposited on two different substrates: film 1 was on stainless steel and film 2 was on silicon. Both films were fabricated by DC diode magnetron sputter deposition.

The NiTi film deposited on stainless steel, film 1, was sputtered at 3.0 mTorr argon pressure, at a substrate temperature of 25°C, cathode power of 250 W, from $Ti_{52}Ni_{48}$ alloy targets. The films were easily peeled from their substrates, as adhesion was very poor. The resulting films where very rough on the surface, with what appeared to be scratches from the stainless steel translating into the same pattern of scratches in the film. They were brittle and dull silver in color. The as-sputtered films were amorphous and approximately 22 microns thick.

The NiTi film deposited on silicon, film 2, was sputtered at 3.0 mTorr argon pressure, at a substrate temperature of 25°C, cathode power of 250 W, from $Ti_{52}Ni_{48}$ alloy targets. This film was diced while still on the silicon substrate and delaminated from the substrate by repeated thermal shock cycles using liquid nitrogen and a hot plate set at 100°C water. The adhesion often caused silicon to be torn off with the peeled film. These films were tough and shiny silver. The as-sputtered films were amorphous and approximately 13 microns thick.

The films were cut with scissors to fit into the ¼ inch diameter aluminum DSC pans. The films were annealed in the DSC under an atmosphere of nitrogen isothermally or isochronally and DSC patterns recorded.

TEM samples have been prepared by the "wedge" method [75]. A stack consisting of a thermally oxidized silicon wafer, NiTi film disc, and no. 1½ glass coverslip were epoxied (EPO-TEK 353nd) together, providing both support for the film and enough surface area to handle the specimen during the sample preparation procedure. The tripod-polished sample was glued to a 3mm Cu grid with M-Bond and successfully ion milled to electron transparency.

TEM was performed on selected films at the National Center for Electron Microscopy (NCEM) [76]. The JEOL 3010, Philips CM200 and the JEOL 200CX Analytical Electron Microscope (AEM) were all used. TEM done at temperatures lower than room temperature were done using a liquid nitrogen cooled double tilt stage in the Philips CM200. Heating experiments done in the AEM utilized the heating, double tilt stage.

4.1   Experimental Outline

Experiments on these films consisted of determination of the dynamic crystallization temperature, as commonly done [53, 77-79] for amorphous materials, by heating the sample at a constant rate of 10K/min (isochronally) in a DSC and measuring heat evolved during the devitrification. The onset of crystallization was used as the upper limit for the study of isothermal annealing experiments. The films were crystallized at progressively lower temperatures until no exothermic crystallization peak could be observed.

TEM was performed on fully transformed films annealed at various temperatures to determine microstructural differences associated with lowering the devitrification

15

temperature. TEM was also performed on films annealed at a specific temperature for various times to elicit the transformation rates. In-situ phase identification experiments by diffraction in the TEM were performed at temperatures between –60ºC and 200ºC of fully transformed samples to determine the temperature/phase relation of the two major grain types, columnar grains and plate-like grains.

5   Results and Discussion

5.1   Devitrification of Film 1

Differential scanning calorimetry (DSC) offers clear evidence of the transformation of the amorphous film to the crystalline state, figure 3. The heating thermogram exhibits one distinct exotherm at 451ºC, which defines the dynamic crystallization temperature, T_x, as 451°C for Film 1. The total energy liberated during the devitrification was about 33J/g, which agrees with reported results [53].

Film 1 was then isothermally annealed at temperatures lower than T_x, starting at 440ºC, with the lowest devitrification temperature at which an exothermic peak could be observed being 420ºC, figure 11. As the annealing temperature was lowered, the crystallization took longer to start (the transient time increased) and the devitrification curve broadened out as expected, according classical nucleation theory of amorphous alloys [68-70, 80].
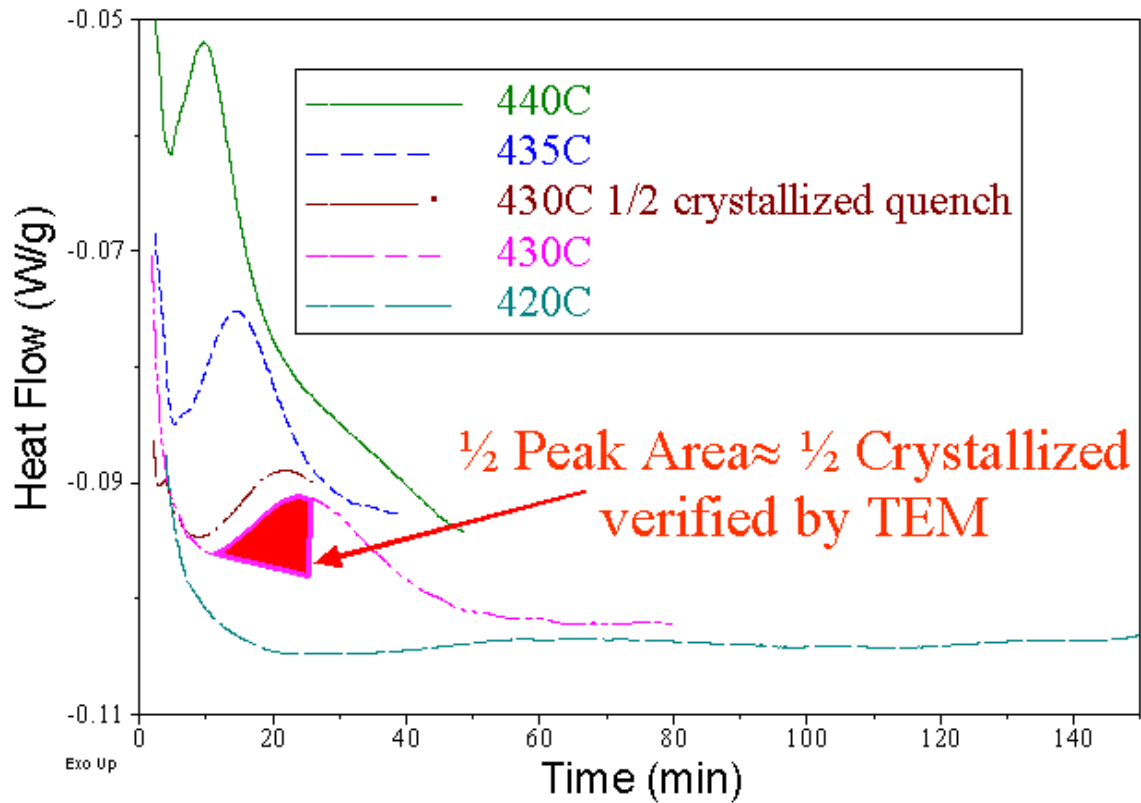
Figure 11: Isothermal DSC measurement of 22μm amorphous equiatomic NiTi film showing broadening of crystallization peaks and increase in transient times for lower temperatures. It appears near 420ºC, crystallization may not be occurring, a fact that must be investigated via TEM.

5.2   Microstructure via TEM of Film 1

The relative area of the crystallization peak should correspond to the amount the sample has transformed [69, 70, 72]. As shown in figure 11, half of the area of the crystallization peak occurred at 25 minutes (shown in red), and should correspond to the film being half crystallized. The cross-sectional microstructure of the sample crystallized for 25 minutes at 430ºC is shown in figure 12 (close-up in figure 13), revealing that the film is 42% crystallized, a value that bodes well with the theory that the relative area under the crystallization curve (the energy liberated) at a particular time relative to the total area under the curve corresponds to the amount the phase transformation has proceeded.

17

The TEM micrograph shown in figure 12 presents one of the two free surfaces where nucleation occurred, followed by grain impingement and finally columnar growth of the grains consuming the amorphous phase. Note that the crystalline/amorphous interface is nearly flat implying the grains grew at nearly the same rate into the amorphous phase. This film was 22.4 μm thick, and thus two surfaces, each 4.7 μm
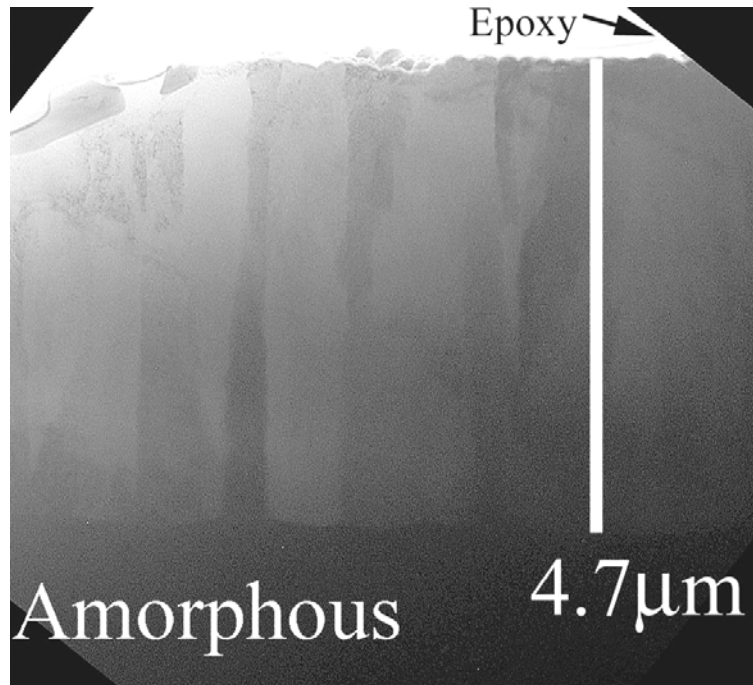
Figure 12: TEM image of one of two surfaces showing crystallization must have occurred at the surface, followed by grain impingement and finally columnar growth of the grains consuming the amorphous phase. Note that the crystalline/amorphous interface is nearly flat implying the grains grew at nearly the same rate into the amorphous phase. This film was 22.4 μm thick, and thus two surfaces, each 4.7 μm thick, represent 42% crystallized product, a value that supports analysis of the DSC curves. This TEM is of the sample labeled "430ºC ½ crystallized quench" in figure 11, which was quenched in liquid nitrogen after 25minutes, or approximately half the peak area observed when the sample is fully crystallized.

thick, represent 42% crystallized product, a value that supports the analysis of the DSC curves. This TEM is of the sample labeled "430ºC ½ crystallized quench" in figure 11, which was quenched in liquid nitrogen after 25minutes, or approximately half the peak area observed when the sample was fully crystallized.

Figure 13 is a close-up of the amorphous/crystalline interface, showing the crystallization front is fairly flat and is consuming the amorphous phase. Also, note the grain size is approximately one micron, a value
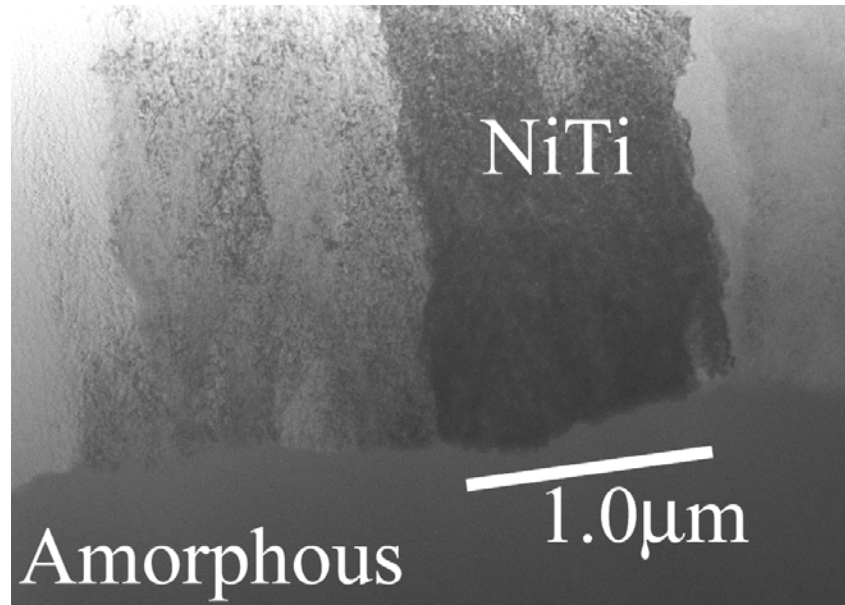
Figure 13: Interface of the same film shown in figure 12. The grain size is approximately 1μm.

often reported in the literature for NiTi films when devitrified from the amorphous state [6, 74, 81].

Because of the film roughness and brittleness, further analysis was not done as a better film, Film 2, was fabricated on a silicon substrate, producing a smoother surface and a more resilient amorphous film.

5.3   Devitrification of Film 2

Film 2 was crystallized in the DSC and the heat evolved during the crystallization was recorded at temperatures starting at 450ºC and annealing as low as 380ºC. Only those films annealed between 420ºC and 450ºC showed a crystallization peak that was able to be resolved in the DSC as presented in figure 14. The heat evolved was between 17-23 J/g for these films. The films annealed at 430ºC, 425ºC and 420ºC showed two crystallization peaks. When adding these two peaks together, the heat evolved was 17 to

19

18 J/g, lower than the 22-23J/g of heat evolved when only one peak was observed. The

lower heat evolved for the three films with dual peaks can be attributed to the fact that

some of the heat was not added in when the two peaks were separated.
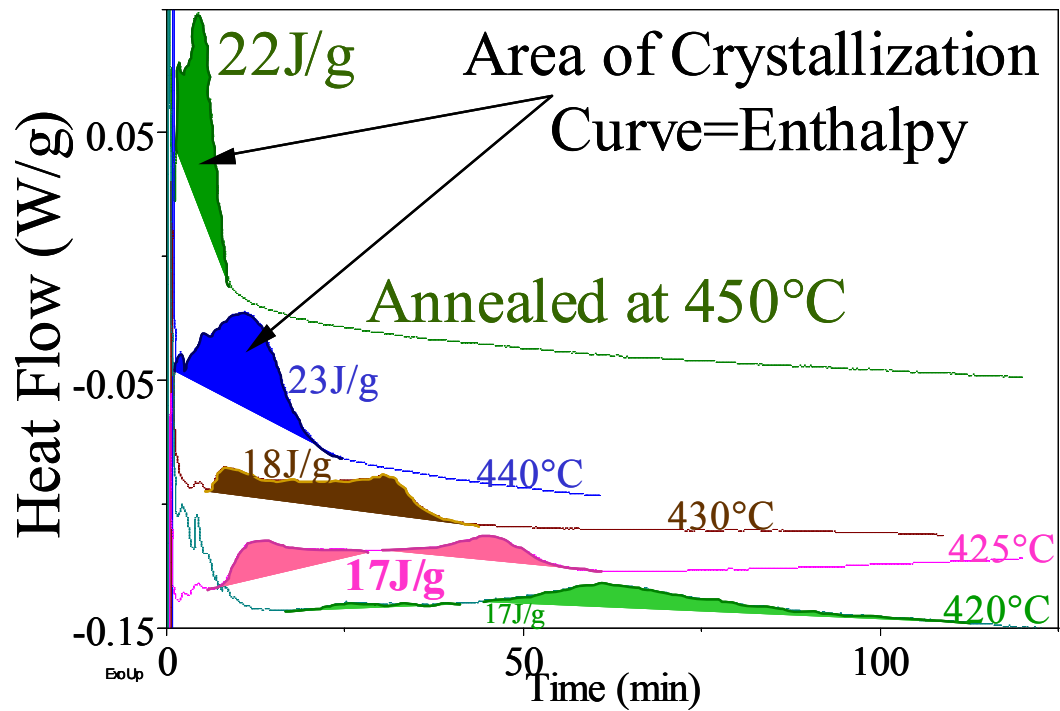
Figure 14: Isothermal anneals of freestanding Film 2 deposited and removed from silicon substrates. The lowest devitrification temperature shown in this figure is 420ºC, but films were annealed to as low as 380ºC and still showed signs of partial crystallization. Note that the devitrification takes longer to start and the peak broadens as the annealing temperature is lowered. Double crystallization peaks imply different parts of the film crystallized at different times.

It is clear from figure 14 that there are two peaks in the crystallization process.

Each peak may correspond to a different part of the film crystallizing as will be discussed

in the ensuing sections.

Figure 15: TEM image of Film 2. Annealed at 420ºC for 200 minutes, this TEM cross-sectional micrograph clearly shows the columnar grains at the top of the image, which nucleated at the surface of the film and consumed the amorphous phase. The grains at the bottom of the image are the platelets, which appear to have nucleated at the interior. Their contrast is more singular, typical of single grains. It is also evident that the platelets are much larger than the columnar grains.

Figure 15 presents a TEM cross-section of film 2 after annealing at 420ºC for 200 minutes. The top of the micrograph shows the columnar grains that nucleated at the surface. The grains at the bottom of the image are large, single contrast platelet grains that transformed in the interior of the film. The interface is flat, indicating that the columnar grains nucleated at the surface, impinged and then grew into the amorphous phase at a constant rate.
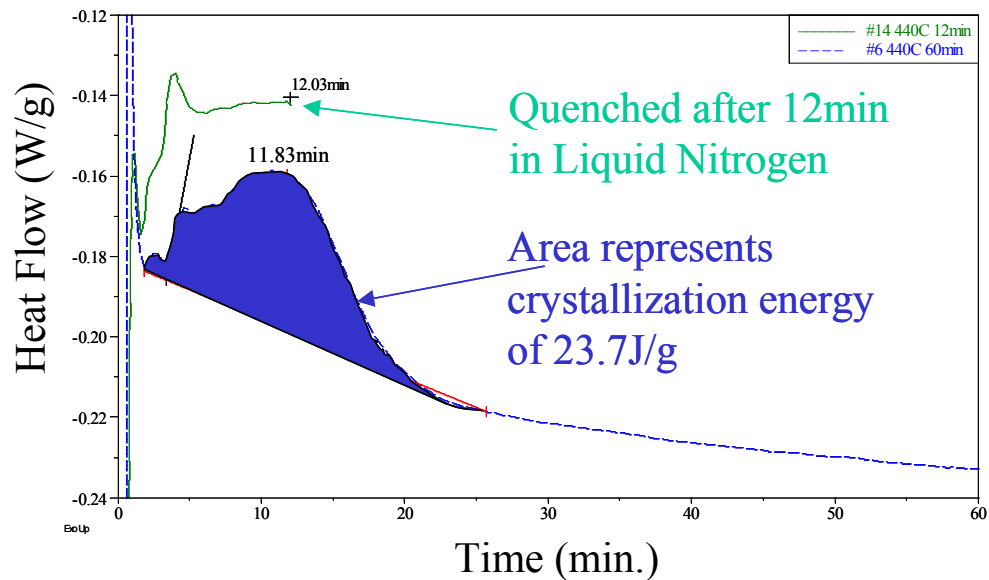
Figure 16: DSC of two films annealed at 440ºC. When crystallized for only 12 minutes, the film did not have time to fully crystallize, as would be expected by looking at the area of the curve.

When an amorphous film was annealed for a shorter time of 12 minutes at 440ºC in the DSC, figure 16, it was observed by cross-sectional TEM that the film did not fully transform, figure 17. The devitrification curve for the film annealed for 60 minutes, presented in figure 16, shows that the film was fully crystalline after 25 minutes (shaded area). Therefore a sample annealed for half of this time should not be fully
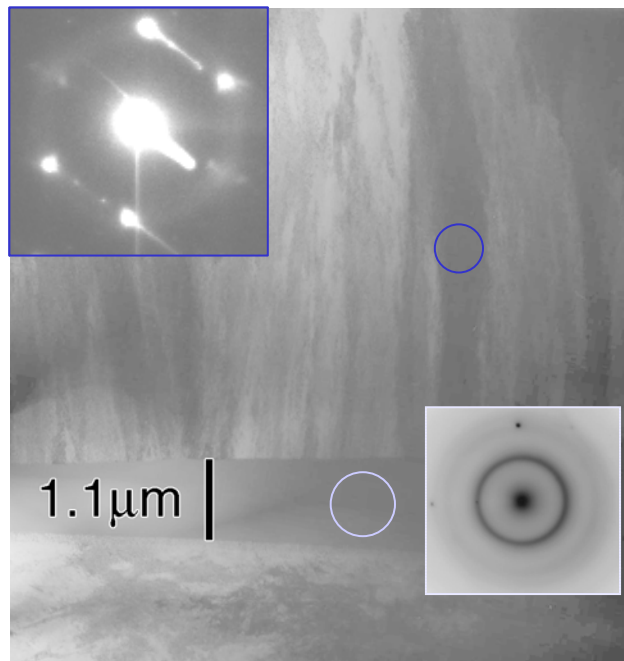
Figure 17: TEM cross-section of film annealed at 440ºC for only 12 minutes. The 1.1 μm thick amorphous layer separates columnar grains layer from the platelet grains. The diffraction patterns confirm that the middle layer is amorphous and the columnar grains are crystalline.

22

crystalline. Indeed, the interior of the film remained amorphous. Observe the amorphous rings in the diffraction pattern presented in figure 17. Notice that the top of the film contains the columnar grains, while the bottom of the TEM image shows the platelet grains. These platelets are roughly in the center of the freestanding film and NOT at the bottom of the film. The amorphous layer separates these two types of grains. This confirmed that the columnar grains nucleate at the surface and grow into the film. It is also verified that the two morphologies form separately from each other. The interior crystallized layer clearly has a different morphology than the surface columnar grains. They also nucleated and grew independently of each other. These two grains nucleated at different times and account for the two peaks observed in the DSC curves taken during crystallization, figure 14.

5.4   Transformational Behavior of Film 2: DSC
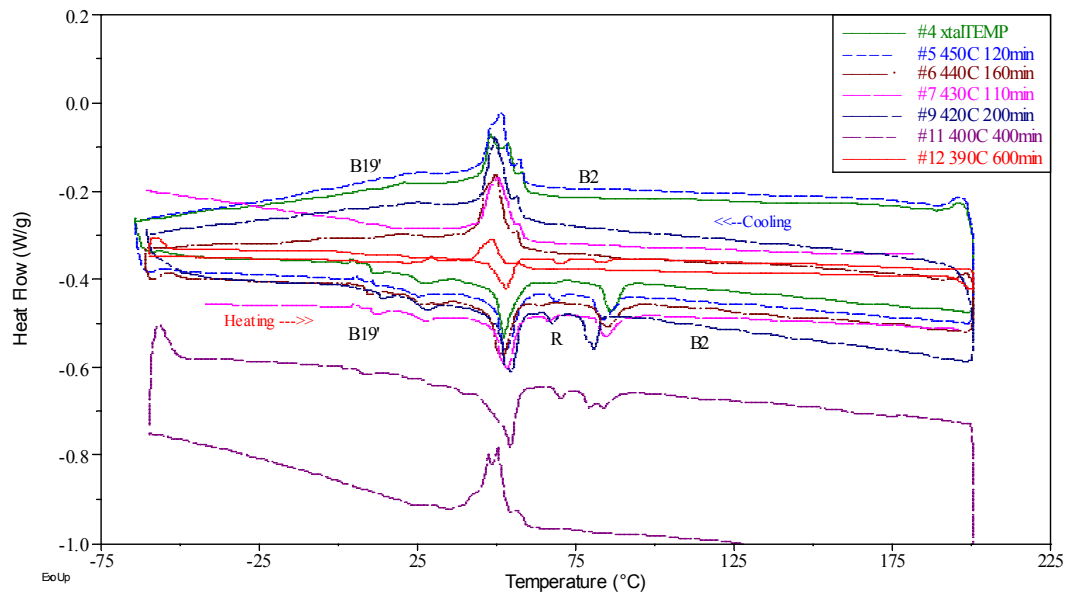
Figure 18: Transformational behavior of NiTi (Film 2) annealed at various temperatures lower than T_x. Films annealed lower than 420°C do not show transformational peak areas as large as those annealed at higher temperatures. The reduced area indicates such films are not fully crystalline. Phase labeling was a first guess and will be shown to be more complicated.

23

The transformational behavior of the crystallized films was subsequently studied by cycling through the temperature range of –60ºC and 200ºC in a DSC while measuring the heat flow. All of the films transformational behavior is presented in figure 18. All the films were repeatedly cycled several times through the temperature range of –60ºC and 200ºC. When the curves were overlaid, they showed the same behavior during each cycle, thus showing that the transformations were completely reversible. Selected data is presented in figure 19, showing the phases that might be present at the various temperatures during heating and cooling. That is that B19' might be present at low temperatures and B2 at higher temperatures with the R phase the intermediate temperature phase. But comparison of this data with the transformational behavior of NiTi reported in the literature showed a discrepancy [22, 33, 53, 55, 63, 79, 82-85].
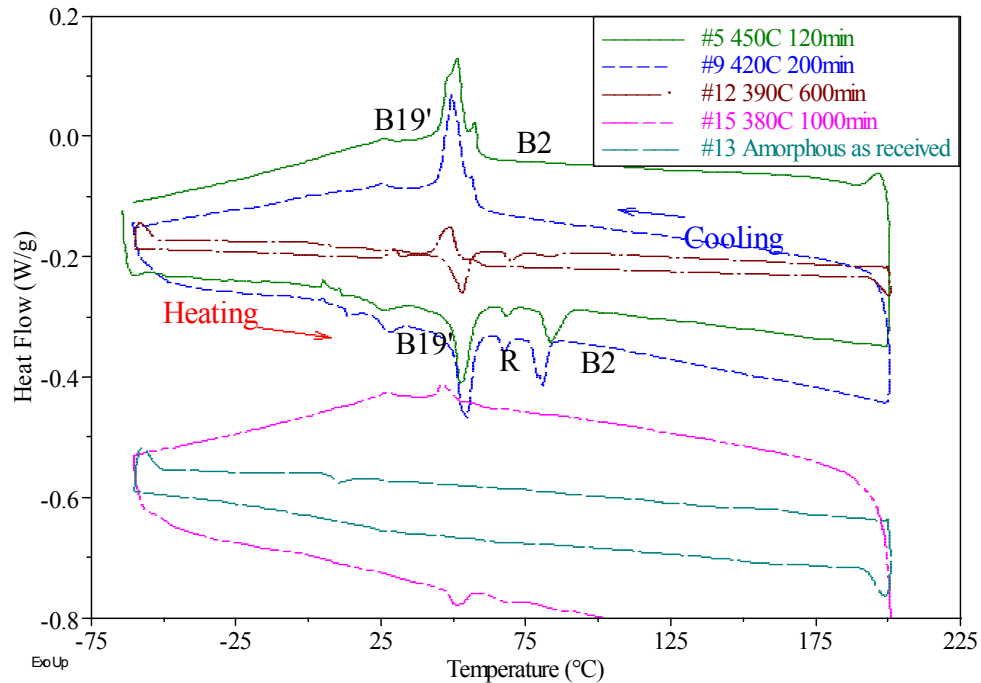
Figure 19: Transformation behavior of Film 2 annealed at high, medium and low temperatures as well as the as-received amorphous film. The film annealed at 390ºC shows a reduced peak area of the phase transformations compared to fully crystallized samples (Sample #5 & #9) indicating the film has not fully transformed to the crystalline state.

Gyobu [55], for example, studied the crystallization of equiatomic films annealed at 470ºC in a DSC, figure 20 [55]. Comparison of the transformational behavior of Film 2 and those reported in the literature [22, 33, 53, 55, 63, 79, 82-85] show that there was a discrepancy in how the R-phase develops. R-phase is always reported as developing during cooling and not during heating, where as the results in figure 18 and figure 19 indicate that R-phase may be present during heating but not cooling. Phase identification via TEM was thus used to determine which peaks corresponded to which phase changes and is presented in Section 5.5.

Figure 20: DSC curves associated with the B2-R-B19 transformations of a Ti–48.6at.% Ni alloy film aged at 743 K for 1.8 ks under constraint after crystallization by holding at 743 K for 0.36 ks [55].

It is evident that as the temperature of crystallization is reduced, there is a point at which the film no longer fully crystallizes. This is shown to be between 390ºC and 420ºC as presented in figure 21. The decreased crystallization peak height of the film annealed at 390ºC for 600 minutes, compared to that annealed at 420ºC for 200 minutes, can be attributed to some of the film remaining amorphous and thus being unable to transform between two solid state phases. This was confirmed by TEM, figure 22, showing that only the surface had transformed when the film was annealed at 390C. Notice that the grains do appear to be columnar. These grains are at the surface of the film, while the amorphous area is at the interior.

25

Figure 21: Reversible phase transformations responsible for shape memory and super-elastic properties of NiTi films. Evident for films annealed from 450ºC to as low as 390ºC. Reduced peak height @ 390ºC indicates not all the film is crystalline compared to those annealed at 420ºC and 450ºC.
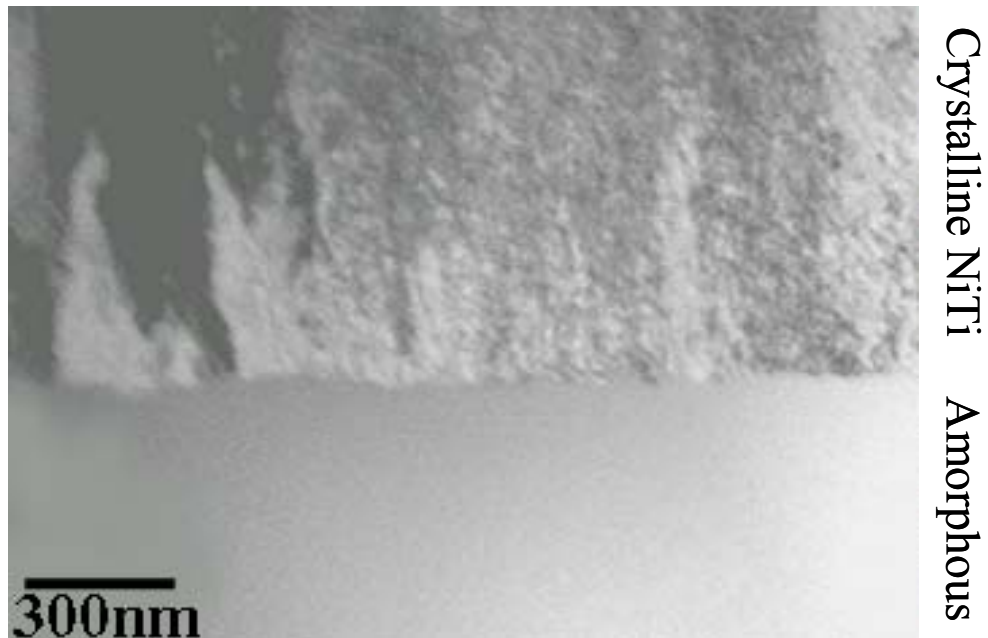
Figure 22: TEM of film crystallized at 390ºC for 600 minutes. The crystalline grains clearly nucleated at the surface (top in image) and consumed the amorphous phase. But the film never fully crystallized and the resulting DSC shown above shows a reduced transformation peak.

5.5   Transformational Behavior of Film 2: In-situ phase ID via TEM

As discussed in section 5.4, the DSC peaks which resulted from solid state phase transformations between B19', B2, and the R phase were shown not to be in the same temperature range as reported in the literature. Thus, an *in-situ* heating and diffraction experiment was used to identify the observed DSC peak. The phases of the columnar and platelet grains were identified by diffraction as a function of temperature.
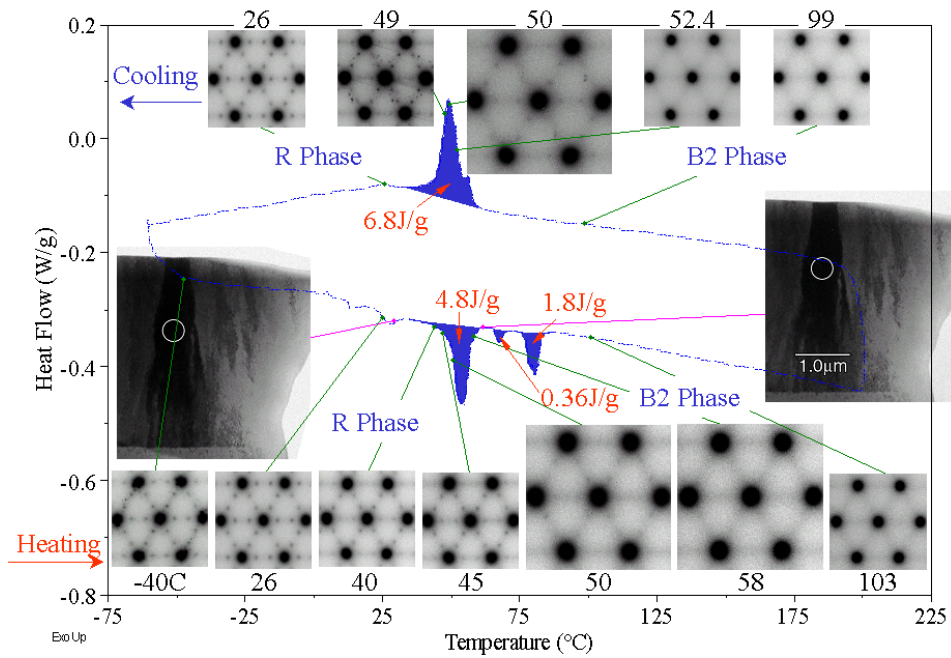
Figure 23: *In-situ* experiments identifying endotherms and exotherms which appear when columnar grains transform from R-phase to B2 phase and back. Included are the grains the diffraction experiment were performed on at low and high temperatures, showing there was no morphological change.

Figure 23 presents the results of the *in-situ* heating experiment for the columnar grains. Many of the diffraction patterns are included in this figure and identified with the temperature at which they were taken. In addition the DSC results and the TEM image are included to show exactly where the aperture was placed on the image and which peaks correspond to which solid state phase transformation. The grains were rotated to a

[111] zone and isolated with a 0.4 micron aperture and diffraction patterns were taken in the [111] zone for the B2 phase.

Figure 23 clearly identifies the phase transformations responsible for the DSC peaks. For example, the 4.8J/g endotherm, which occurs upon heating at 52ºC, is due to the phase transformation from the R-phase to B2. Notice that at 45ºC, spots appear at 1/3 the major $\langle \overline{1}10 \rangle$ spots due to the rhombohedral phase. As the temperature is raised past the 4.8J/g endotherm, the extra spots grow faint (see the diffraction pattern at 50ºC) until they are no longer present at all at 58ºC. The temperature of this endotherm corresponds well with that reported [33, p. 699] for R to B2 transformation, as does the exotherm. The energy associated with a phase change on cooling has been reported to be ~-3.0J/g (exothermic), which bodes well with the value reported here of an endotherm of 4.8J/g seen on heating [4, p. 991].

Upon cooling, the reverse phase transformation is evident in the columnar grains by the appearance of the extra reflections, when cooled below 52.4ºC.

Further analysis of figure 23 shows that the columnar grains do not go through any phase transformation upon heating in the temperature range of 58ºC and 100ºC. Thus the smaller two peaks at the bottom of the figure are not due to this type of grain transforming. Thus the columnar grains transform only between B2 and B19'.

When the endotherms are added up (4.8+0.3+1.8=6.9J/g) and compared to the exothermic reactions (6.8J/g), it is clear that the energy is conserved and that the transformations are fully reversible. Measuring the same curve five times and observing that all curves are the same also substantiates the reversibility of the solid-state reactions.

28

A similar experiment was performed on the platelet grains and this experiment is summarized along with the results of the columnar grains in figure 24. The platelet grains are observed to be martensitic (B19') up to 80C and then transform to austenite (B2) above this when heated. This is determined by the disappearance of the spots at 1/2 the major $\langle \bar{1}10 \rangle$ spots. When the film was cooled, the phase actually transformed to the R phase, not back to the austenitic phase.
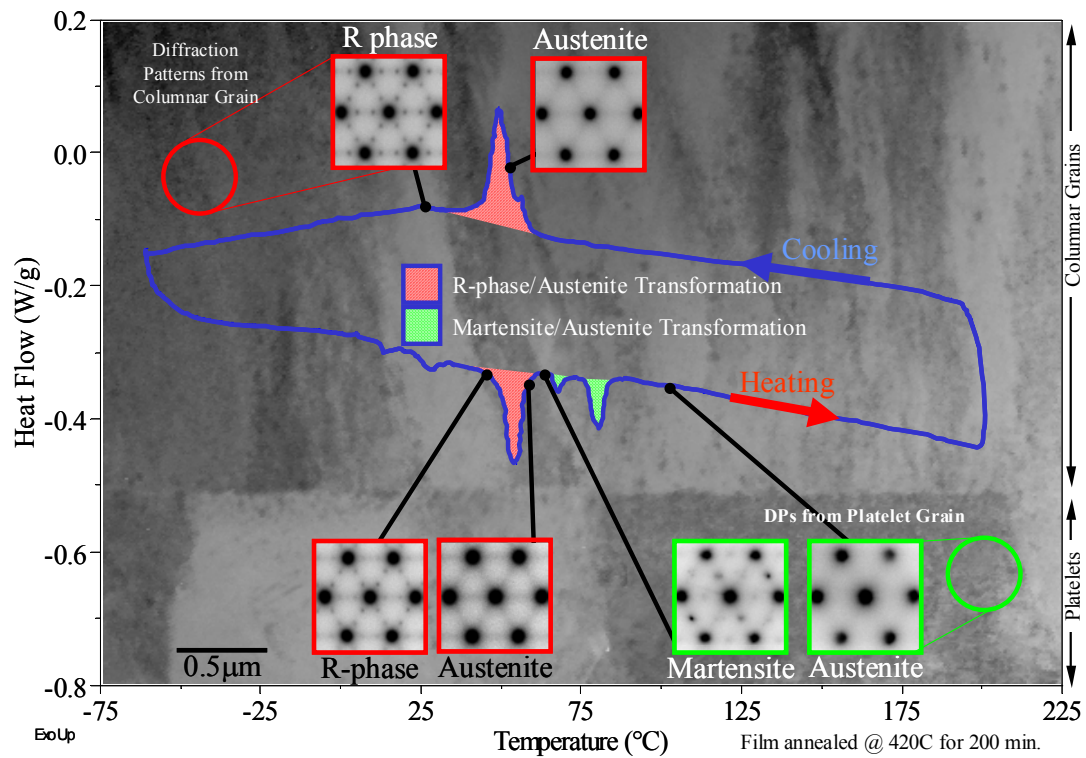
Figure 24: The phase transformation of columnar grains and platelet grains was studied in-situ. The R to B2 phase transformation is attributed to the columnar grains while the B19' to B2 is attributed to the platelet grains.

Comparison of the small area of the austenite/martensite peaks with the larger area of the R-phase/austenite peaks reveals that most of the material transforms between R and B2 phases. This may be due to the low temperatures at which these films were crystallized.
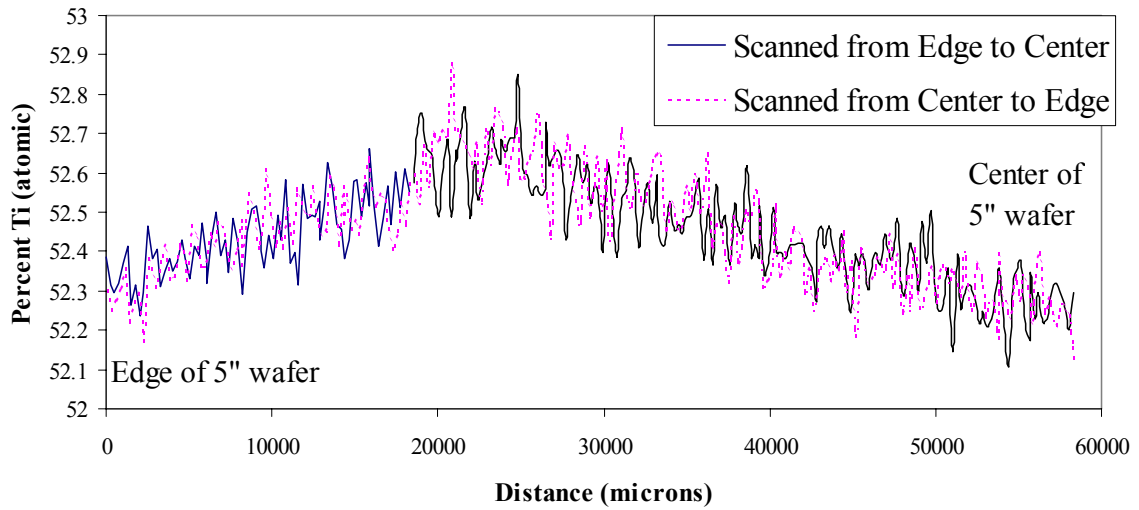
**Figure 25: MicroProbe analysis showing composition variation across a film deposited on a 5"
diameter (63.5mm radius) wafer. This film was deposited with the same conditions as Film 2 and
thus corresponds to the same composition and variation across the wafer. The error of the absolute
composition can be as large as one atomic percent, while the changes in composition across the wafer
are on the order of 0.2at.%.   Thus the observed maximum Ti composition can be and trusted to be
near 25mm from the edge. Samples studied were taken from all over the wafer and thus there will be
some compositional difference in samples.**

Figure 25 presents microprobe analysis showing composition variation across a

nearly equiatomic NiTi film deposited on a 5" diameter (63.5mm radius) silicon wafer.

This film was deposited with the same conditions as Film 2 and thus corresponds to the

same composition and variation across the wafer. The atomic percent of titanium is

plotted as a function of position, where zero corresponds to the edge of the wafer. The

balance is Ni. The analysis was done by scanning once from center to edge (broken line)

and then again from edge to center (solid line) to show that the trend was repeatable. The

noise thus can be clearly seen to be about 0.2 atomic percent by observing the variations

in composition at the same place on the wafer. The error of the absolute composition for

microprobe analysis can be as large as one atomic percent [86-89], and thus is only a

starting point for compositional determination. The observed maximum Ti composition,

however, can be trusted to be between 20 and 30mm from the edge. Samples studied were taken from all over the wafer and thus there will be some compositional difference in samples, as much as 0.5 at.%.

5.7 Composition of Columnar and Platelet Grains by EDX in the TEM

Because the columnar grains transform differently than the platelet grains, it was desired to determine if there was any compositional differences in these two types of grains. It was determined that there was no compositional difference between the columnar grains and the platelets by using Energy Dispersive X-ray spectroscopy, using a large probe (but much smaller than the grain) on each of the grains. Analysis of this spectrum then yielded the composition. Two of the spectra collected are presented in figure 26. No difference in composition was apparent between the two grain types.
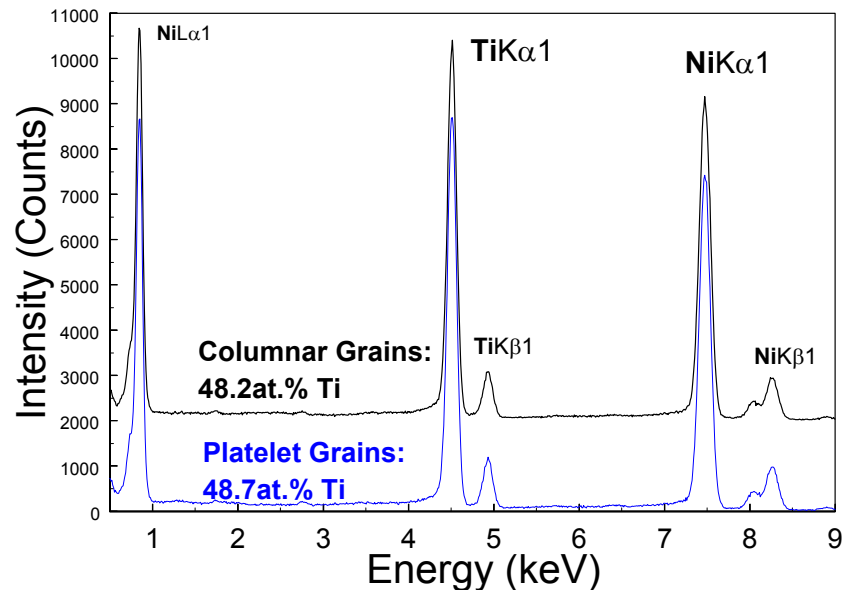
Figure 26: An example of an Energy Dispersive X-ray spectrum of a columnar grain and a platelet grain, showing that there is a negligible difference in composition, which is within the error of the measurement. Several such spectrum were taken and no notable difference in the composition of the two types of grains was observed.

31

5.8 Particles at the Interface: EELS and Nanoprobe Analysis

Analysis of the interface between the columnar grains and the platelet grains presented in figure 15 shows that particles form at this interface, which will be shown to be titanium rich. It was also determined that the interface itself was rich in titanium. This was determined from nanoprobe line scans across the interface, line scans across particles and Electron Energy Loss Spectroscopy of the interface.
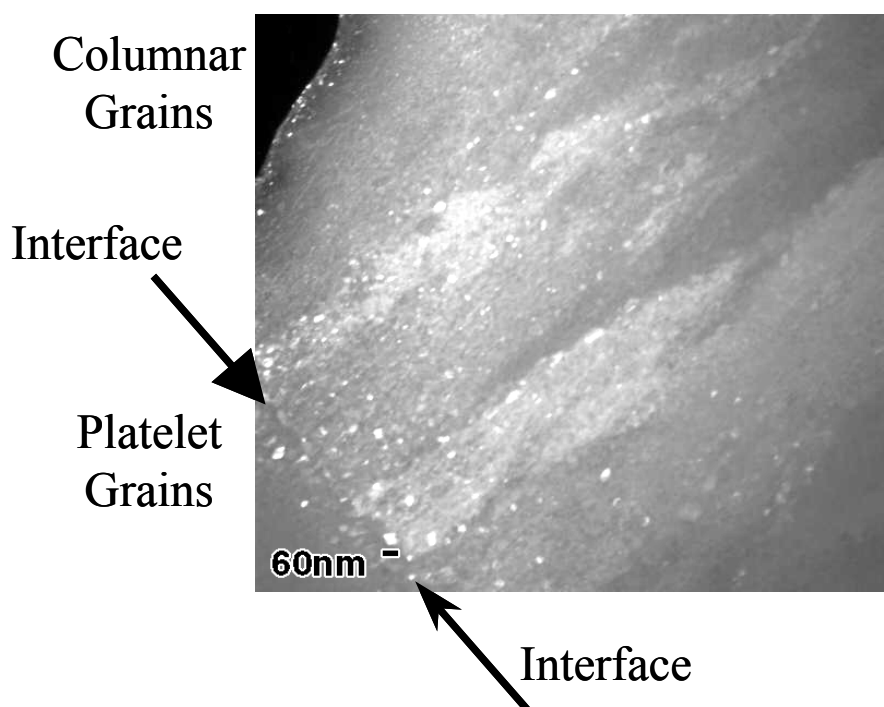
Figure 27: Dark field of interface between columnar grains and platelets for the film annealed at 420C for 200 minutes. Note that some of the particles show up bright, indicating a texture in the film.

Figure 27 presents a dark field image of the interface showing the particles are about 10 to 60nm in size. The interface is not horizontally inclined, but marked with arrows for clarity. It appears that the particles are most numerous at the interface.

Elemental mapping was used to show two-dimensional distributions of Ni and Ti. This was done by recording two images, one before and one after the ionization edge and dividing the post-edge image by the pre-edge image. The resulting *jump ratio image*

yields contrast due to elemental distribution only, with thickness and diffraction contrast eliminated [90(p.331)]. Bright and dark contrast in a jump ratio image show where elemental concentration is high or low.
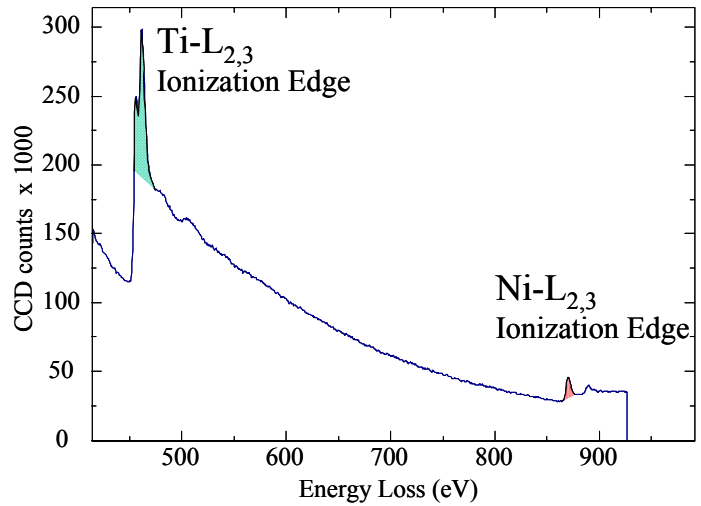
The EELS spectrum taken from the interface is presented in figure 28. Contrast was established by taking

Figure 28: EELS Spectrum from the interface of the film annealed at 420C for 200 minutes used to create the Ni and Ti jump ratio maps. The post-ionization edge image was divided by the pre-ionization edge image to yield jump ratio images for both Ni and Ti. Bright contrast shows where that element has higher concentrations than other areas in the image, while darker contrast shows where that particular element is deficient.

images with the pre-edge and post-edge energies. These two images were then used to make *jump ratio images*. The ionization edges for Ni and Ti are labeled. The jump ratio images are shown in figure 29. They clearly show the interface and particles are rich in titanium and depleted in nickel.
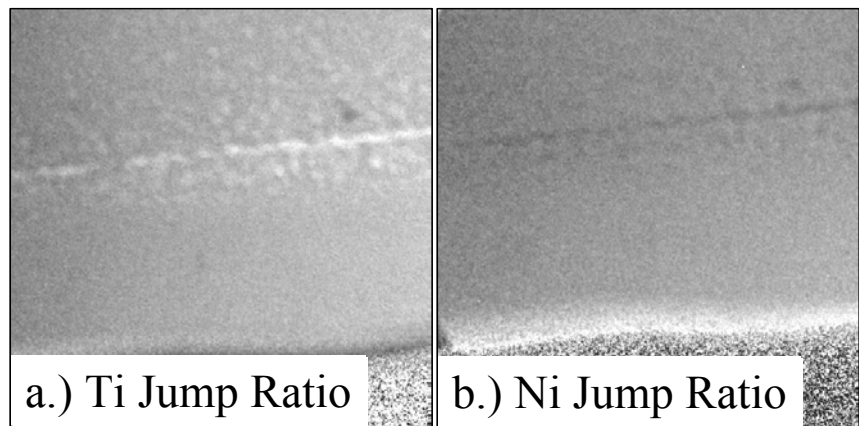
Figure 29: Jump ratio images for Ni and Ti. The bright contrast in a.) shows that the interface and particles are rich in titanium while the same areas are shown in b.) to be depleted of Ni because of the dark contrast.

Further support of the titanium rich particles was found by performing a nanoprobe line-scan across a particle at the interface. A probe 1.4nm large was used to take fifty individual energy dispersive x-ray spectrum, similar to the two presented in figure 26. The TEM image exactly where the line scan was taken is shown in figure 30. An example of how the cumulative counts in the Ni $K_{\alpha 1}$ and Ti $K_{\alpha 1}$ peaks are measured (red energy window in the x-ray spectrum) and then plotted as a function of position in the line-
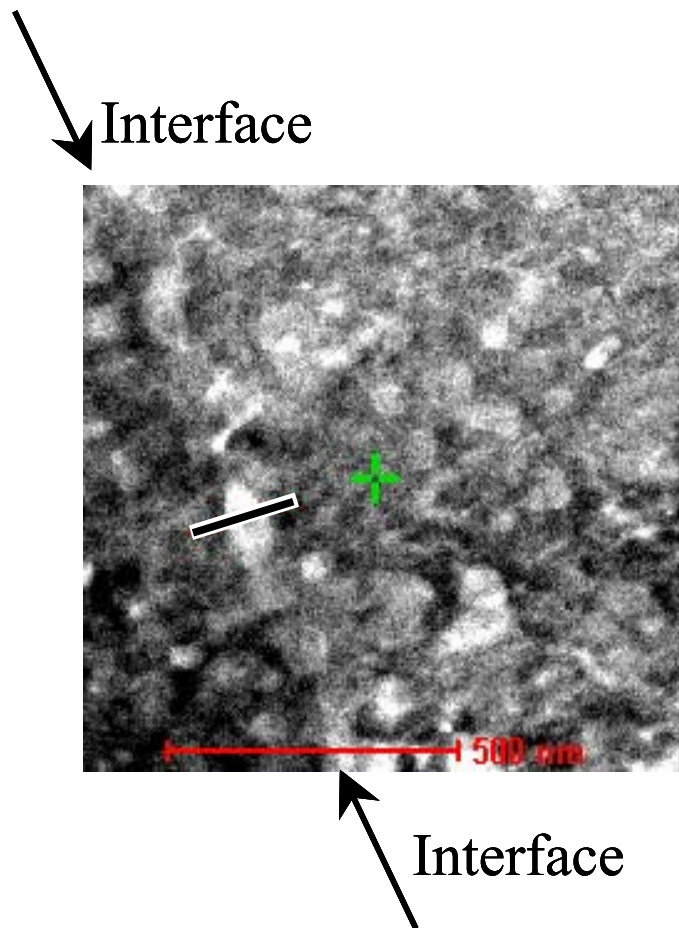
Figure 30: Line scan (black with white border) across a particle (white contrast) at the interface (shown by arrows). Fifty EDX spectrum were taken along this line to analyze composition changes across the interface.

scan is presented in figure 31. Because of the linear relationship between counts measured in the $K_{\alpha 1}$ peaks and composition, counts can be correlated to the composition by analyzing two spectrum along the line scan. The resulting plot of the intensity from titanium and nickel signals as a function of position is presented in figure 32. Intensity was converted to composition and is presented in figure 33. These plots conclusively show that the particles are titanium rich at about 55at% titanium and depleted in nickel. Caution must be taken with this measured composition as the particles are in the

34

surrounding matrix. Hence there is still a significant x-ray signal from the background,

which is nearly equiatomic. Therefore, it is expected that the particle composition is

actually more rich in titanium and likely to be the commonly observed Ti_2Ni [91].
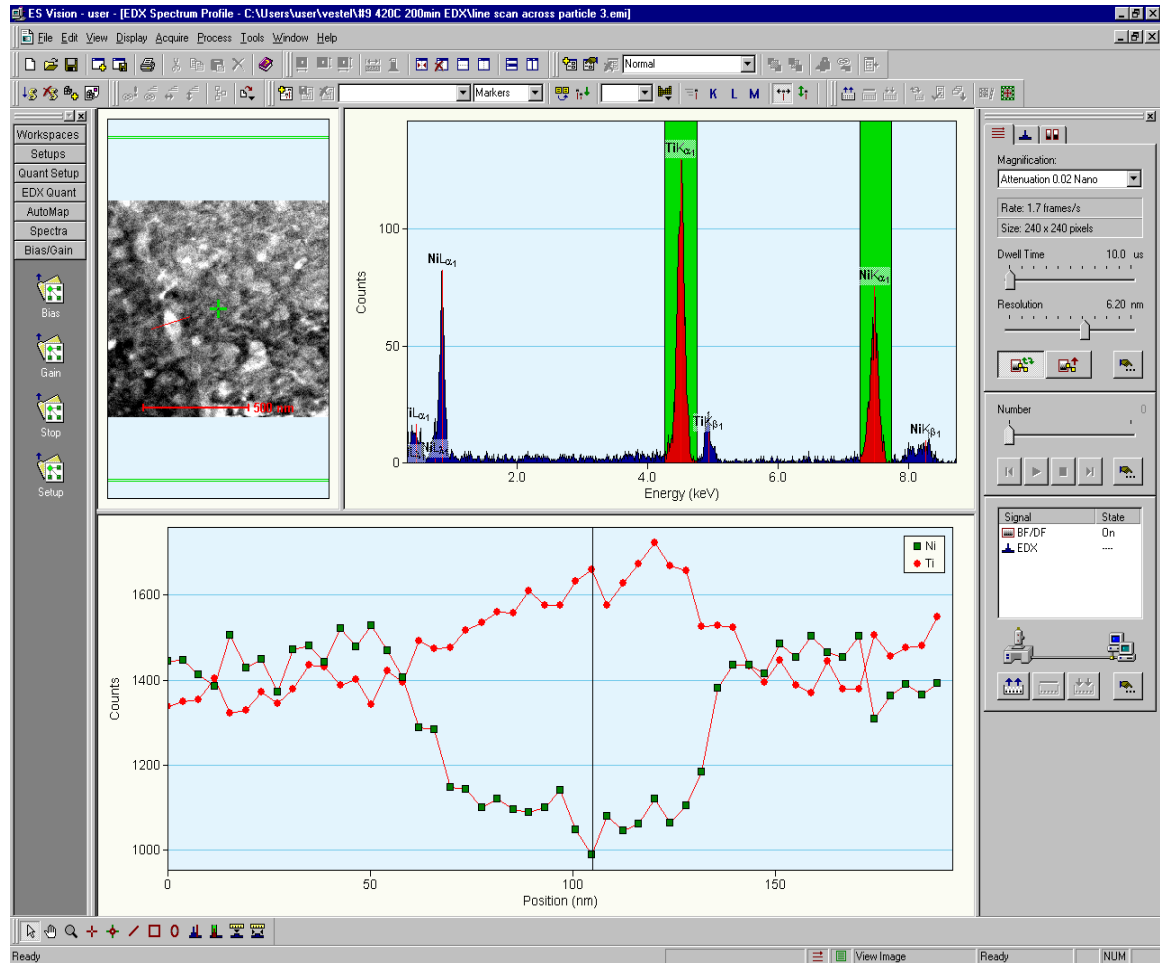
Figure 31 Example of how the cumulative counts in the Ni $K_{\alpha 1}$ and Ti $K_{\alpha 1}$ x-ray peaks are measured (highlighted in red in the x-ray spectrum) to yield a plot of counts vs. position for the line scan. Analysis on two of the points correlates counts with composition and allows figure 33 to be plotted.
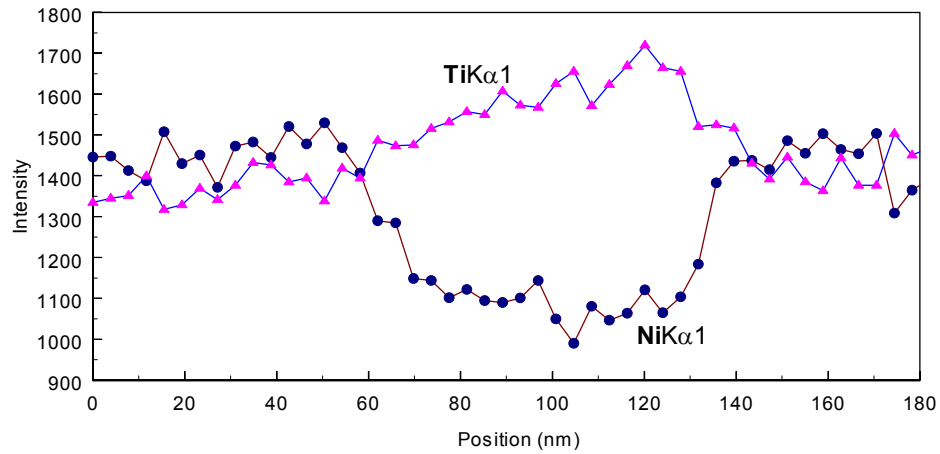
Figure 32: Line scan result for the Ti and Ni composition across the particle at the interface.
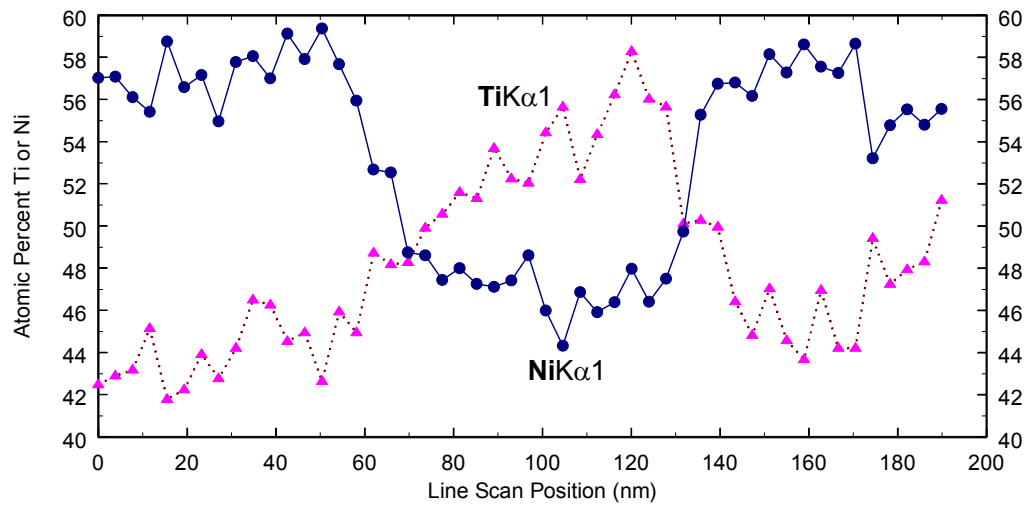
Figure 33: Line scan replotted with composition on the ordinate axis. The particle starts at about 70nm into the line scan and ends at about 130nm. Clearly the particle is titanium rich and Ni depleted.

6   Conclusions

NiTi films sputter deposited at 25°C were amorphous. These films were released and then crystallized in a DSC. It was found that as the crystallization temperature was lowered from 450°C to 400°C, the incubation time increased and the crystallization peaks broadened, but the films fully crystallized. When the same films were subjected to an annealing temperature of 390°C, they did not fully crystallize.

Two crystallization peaks were observed and attributed to two types of grain morphologies, columnar grains and platelet grains. It was determined that the columnar grains nucleated at both free surfaces and grew laterally until they impinged, covering both surfaces. at the surface. These grains then grew into the amorphous phase, consuming it at a constant rate, producing a flat amorphous/crystalline interface. The platelet grains were shown to nucleate separately in the interior of the film.

The two types of grains were shown to undergo different phase transformations when cycled through the temperature range of –60ºC and 200ºC. It was observed that the columnar grains transformed between the rhombohedral phase and the austenitic phase. The platelets were shown to transform between martensite and austenite. No compositional difference could be detected between the columnar and platelet grains.

EELS was used to examine the composition of particles observed at the interface between the two types of grains as well as the composition of the intergranular interfaces. It was found that Ti_2Ni particles resided in a high concentration near the interface and the interface was titanium rich.

Low temperature, post processing crystallization anneals have been shown to successfully crystallize freestanding NiTi films. Such low annealing temperatures would be favorable for their CMOS compatibility and thus are important to the applications of MEMS structures.

7   Appendix

7.1   Derivation of the Clausius-Clapeyron Equation

A quasi-static thermodynamic formalism of the small volume, shear phase change endured by equiatomic TiNi. The internal energy (U) has been shown [92] to be a detailed energy balance:

$$dU = \underbrace{TdS - pdV}_{\text{Heat}(dq)+\text{work}(dw)} \underbrace{\underbrace{-T\delta S_i - \delta W_i}_{\text{Dissipative entropy/work}} \underbrace{-dE_{elastic}}_{\text{Stored strain}}}_{\text{For ideal thermoelastic behavior all zero}} + \underbrace{V_0 \sigma d\varepsilon}_{\substack{\text{Mech work by} \\ \text{external force}}}$$

$$\tag{1}$$

where S and V are the entropy and molar volume of the two phase system and the other terms are defined above. The Gibbs free energy becomes:

$$G = U + PV - TS - V_0 \sigma \varepsilon \tag{2}$$

$$dG = dU + pdV + Vdp - TdS - SdT - V_0 \sigma d\varepsilon - V_0 \varepsilon d\sigma$$

$$dG = TdS - pdV + pdV + Vdp - TdS - SdT - V_0 \sigma d\varepsilon - V_0 \varepsilon d\sigma + V_0 \sigma d\varepsilon$$

Upon cancellation, assumptions from equation (1) and assuming constant pressure we have:

$$dG = -SdT - V_0 \varepsilon d\sigma \tag{3}$$

Thus, the only way to maintain equilibrium between the low temperature martensite and high temperature austenite during changes in the applied stress is for the transition temperature to change. If the martensite and austenite phases are in equilibrium, we have:

$$dG^M = -S^M dT - V_0 \varepsilon^M d\sigma$$
$$dG^A = -S^A dT - V_0 \varepsilon^A d\sigma \qquad (4)$$

If martensite and austenite are in equilibrium, $G^M = G^A$ therefore $dG^M = dG^A$

and

$$-S^A dT - V_0 \varepsilon^A d\sigma = -S^M dT - V_0 \varepsilon^M d\sigma$$

$$-V_0(\varepsilon^M - \varepsilon^A) d\sigma = (S^M - S^A) dT$$

And the change in the transformation temperature with uniaxial stress required to maintain equilibrium between the martensite and austenite is given by the Clausius-Clapeyron equation:

$$\frac{dT_0(\sigma)}{d\sigma} = -V_0 \frac{(\varepsilon^M - \varepsilon^A)}{(S^M - S^A)} = -V_0 \frac{(\Delta \varepsilon_{A \to M})}{(\Delta S_{A \to M})} \qquad (5)$$

Because $G = H - TS$, or $\Delta G = \Delta H - T\Delta S = 0$ for the equilibrium case,

$\Delta S = \dfrac{\Delta H}{T_0(\sigma = 0)}$ can be substituted into equation (5).

$$\frac{dT_0(\sigma)}{d\sigma} = -V_0 \frac{(\Delta \varepsilon_{A \to M})}{(\Delta H_{A \to M})} T_0(0) \qquad (6)$$

7.2   Sample Calculations for NiTi

$$V_0[\text{m}^3/\text{mole}] = \frac{(47.9+58.7)\text{g}}{2 \text{ mole}} \frac{\text{cm}^3}{6.45g} = 8.26 \text{ cm}^3/\text{mole}$$

$$T_0(0) = (Ms_{\sigma=0} - As_{\sigma=0})/2$$

for a 50Ni-50Ti sample [93],

$$\Delta H_{A \to M (exothermic)} = -20\frac{J}{g} = -20\frac{J}{g} \bullet \frac{53.3g}{mole} = -1066\frac{J}{mole},$$

$$\Delta S = 0.1\tfrac{J}{g \cdot K} = 0.1\tfrac{J}{g \cdot K} \cdot \tfrac{53.3g}{mole} = 5.33\tfrac{J}{mole \cdot K}, \; T_0 = 290K, \; \Delta\varepsilon = \varepsilon_M - \varepsilon_A = \varepsilon_M =\sim 4.5\% = 0.045$$

$$\frac{dT_0(\sigma)}{d\sigma} = \text{-8.26 cm}^3/\text{mole}\frac{(0.1)}{(\text{-1066}\frac{J}{mole})}290K = 0.23\frac{K}{MPa}$$

Alternatively, we could use equation (5)

$$\frac{dT_0(\sigma)}{d\sigma} = -V_0\frac{(\Delta\varepsilon_{A \to M})}{(\Delta S_{A \to M})} = \text{-8.26 cm}^3/\text{mole}\frac{(0.1)}{(\text{-5.33}\frac{J}{mole \times K})} = 0.15\frac{K}{MPa}$$

Note that $\dfrac{J}{cm^3} = MPa$. The

So the transformational temperature, M_s for example, moves up 1K (or 1°C) for

each 4-7MPa of applied stress, values which have been observed by Grummon [56].

8   References

[1]   K. Otsuka and C. M. Wayman, *Shape Memory Materials*. Cambridge: Cambridge University Press, 1998.

[2]   T. W. Duerig and K. N. Melton, "Diffuse yield drop and snap action in a Ni-Ti alloy," presented at Shape-Memory Materials and Phenomena - Fundamental Aspects and Applications Symposium, Boston, MA, USA, 1991.

[3]   W. J. Moberly, J. D. Busch, A. D. Johnson, and M. H. Berkson, "In situ HVEM of crystallization of amorphous TiNi thin films," presented at Phase Transformation Kinetics in Thin Films Symposium, Anaheim, CA, USA, 1991.

[4]   L. Hou and D. S. Grummon, "Transformational superelasticity in sputtered titanium-nickel thin films," *Scripta Metallurgica et Materialia*, vol. 33, pp. 989-995, 1995.

[5]   D. S. Grummon, T. LaGrange, and J. Zhang, "Processing and deployment of sputtered thin films of NiTi and NiTiX alloys for biomedical and MEMs applications," presented at Proc. SMST (invited paper in review), Alisomar, California, 2000.

[6]   S. Kajiwara, K. Ogawa, T. Kikuchi, T. Matsunaga, and S. Miyazaki, "Formation of nanocrystals with an identical orientation in sputter-deposited Ti-Ni thin films," *Philosophical Magazine Letters*, vol. 74, pp. 395-404, 1996.

[7] S. Miyazaki, K. Nomura, A. Ishida, and S. Kajiwara, "Recent developments in sputter-deposited Ti-Ni-base shape memory alloy thin films," presented at IVth European Symposium on Martensitic Transformations, ESOMAT '97, Enschede, Netherlands, 1997.

[8] S. Kajiwara, T. Kikuchi, K. Ogawa, T. Matsunaga, and S. Miyazaki, "Strengthening of Ti-Ni shape-memory films by coherent subnanometric plate precipitates," *Philosophical Magazine Letters*, vol. 74, pp. 137-44, 1996.

[9] L. Chang and D. S. Grummon, "Phase transformations in sputtered thin films of $Ti_x(Ni,Cu)_{1-x}$ II: Displacive transformations," *Philosophical Magazine A (Physics of Condensed Matter: Structure, Defects and Mechanical Properties)*, vol. 76, pp. 191-219, 1997.

[10] K. Najafi and K. D. Wise, "An implantable multielectrode array with on-chip signal processing," *IEEE Journal of Solid-State Circuits*, vol. SC-21, pp. 1035-44, 1986.

[11] J. Chen and K. D. Wise, "A multichannel neural probe for selective chemical delivery at the cellular level," presented at Solid-State Sensor and Actuator Workshop Technical Digest Solid-State Sensor and Actuator Workshop, Hilton Head Island, SC, USA, 1994.

[12] L. Lin and A. P. Pisano, "Silicon-processed microneedles," *Journal of Microelectromechanical Systems*, vol. 8, pp. 78-84, 1999.

[13] N. H. Talbot and A. P. Pisano, "Polymolding: two wafer polysilicon micromolding of closed-flow passages for microneedles and microfluidic devices," presented at Solid-State Sensor and Actuator Workshop Technical Digest Solid-State Sensor and Actuator Workshop, Hilton Head Island, SC, USA, 1998.

[14] J. Brazzle, D. Bartholomeusz, R. Davies, J. Andrade, R. A. van Wagenen, and A. B. Frazier, "Active microneedles with integrated functionality," presented at Solid-State Sensor and Actuator Workshop (TRF Cat. No.00TRF-0001) Technical Digest. Solid-State Sensor and Actuator Workshop, Hilton Head Island, SC, USA, 2000.

[15] I. Papautsky, J. Brazzle, H. Swerdlow, and A. B. Frazier, "A low-temperature IC-compatible process for fabricating surface-micromachined metallic microchannels," *Journal of Microelectromechanical Systems*, vol. 7, pp. 267-73, 1998.

[16] I. Papautsky, A. B. Frazier, and H. Swerdlow, "A low-temperature IC-compatible process for fabricating surface-micromachined metallic microchannels," presented at The Tenth Annual International Workshop on Micro Electro Mechanical Systems. An Investigation of Micro Structures, Sensors, Actuators, Machines and Robots (Cat. No.97CH36021) Proceedings IEEE, Nagoya, Japan, 1997.

[17] J. D. Brazzle, I. Papautsky, and A. B. Frazier, "Fluid-coupled hollow metallic micromachined needle arrays," presented at Microfluidic Devices and Systems, Santa Clara, CA, USA, 1998.

[18] I. Papautsky, J. Brazzle, T. Ameel, and A. Bruno Frazier, "Laminar fluid behavior in microchannels using micropolar fluid theory," presented at IEEE Eleventh Annual International Workshop on Micro Electro Mechanical Systems An Investigation of Micro Structures, Sensors, Actuators, Machines and Systems, Heidelberg, Germany, 1998.

[19] S. Henry, D. V. McAllister, M. G. Allen, and M. R. Prausnitz, "Micromachined needles for the transdermal delivery of drugs," presented at IEEE. Eleventh Annual International Workshop on Micro Electro Mechanical Systems. An Investigation of Micro Structures, Sensors, Actuators, Machines and Systems (Cat. No.98CH36176) Proceedings IEEE Eleventh Annual International Workshop on Micro Electro Mechanical Systems An Investigation of Micro Structures, Sensors, Actuators, Machines and Systems, Heidelberg, Germany, 1998.

[20] A. E. Franke, "Polycrystalline silicon-germanium films for integrated microsystems," in *Ph.D. Electrical Engineering and Computer Sciences*. Berkeley: University of California, Berkeley, 2000.

[21] L. Haji, P. Joubert, M. Guendouz, N. Duhamel, and B. Loisel, "Substrate effects on the kinetics of solid phase crystallization in α-Si," presented at Phase Transformation Kinetics in Thin Films Symposium, Anaheim, CA, USA, 1991.

[22] J. J. Kim, P. Moine, and D. A. Stevenson, "Crystallization behavior of amorphous Ni-Ti alloys prepared by sputter deposition," *Scripta Metallurgica*, vol. 20, pp. 243-8, 1986.

[23] W. L. Benard, H. Kahn, A. H. Heuer, and M. A. Huff, "A titanium-nickel shape-memory alloy actuated micropump," presented at 1997 International Conference on Solid-State Sensors and Actuators. Digest of Technical Papers (Cat. No.97TH8267) Proceedings of International Solid State Sensors and Actuators Conference (Transducers '97), Chicago, IL, USA, 1997.

[24] W. L. Benard, H. Kahn, A. H. Heuer, and M. A. Huff, "Thin-film shape-memory alloy actuated micropumps," *Journal of Microelectromechanical Systems*, vol. 7, pp. 245-51, 1998.

[25] H. Kahn, W. L. Benard, M. A. Huff, and A. H. Heuer, "Titanium-nickel shape memory thin film actuators for micromachined valves," presented at Materials for Mechanical and Optical Microsystems Symposium Materials for Mechanical and Optical Microsystems Symposium, Boston, MA, USA, 1996.

[26] H. Kahn, M. A. Huff, and A. H. Heuer, "Heating effects on the Young's modulus of films sputtered onto micromachined resonators," presented at Symposium Microelectromechanical Structures for Materials Research. Symposium, San Francisco, CA, USA, 1998.

[27] H. Kahn, M. A. Huff, and A. H. Heuer, "The TiNi shape-memory alloy and its applications for MEMS," *Journal of Micromechanics and Microengineering*, vol. 8, pp. 213-21, 1998.

[28] C. L. Shih, B. K. Lai, H. Kahn, S. M. Phillips, and A. H. Heuer, "A robust co-sputtering fabrication procedure for TiNi shape memory alloys for MEMS," *Journal of Microelectromechanical Systems*, vol. 10, pp. 69-79, 2001.

[29] R. H. Wolf and A. H. Heuer, "TiNi (shape memory) films silicon for MEMS applications," *Journal of Microelectromechanical Systems*, vol. 4, pp. 206-12, 1995.

[30] J. A. Walker, K. J. Gabriel, and M. Mehregany, "Thin-film processing of TiNi shape memory alloy," presented at 5th International Conference on Solid-State Sensors and Actuators and Eurosensors III, Montreux, Switzerland, 1989.

[31] P. Krulevitch, A. P. Lee, P. B. Ramsey, J. C. Trevino, J. Hamilton, and M. A. Northrup, "Thin film shape memory alloy microactuators," *Journal of Microelectromechanical Systems*, vol. 5, pp. 270-82, 1996.

[32] P. Krulevitch, A. P. Lee, P. B. Ramsey, J. Trevino, and M. A. Northrup, "Thin film shape memory alloy microactuators," presented at 1996 International Mechanical Engineering Congress and Exposition Micro-Electro-Mechanical Systems (MEMS). 1998 International Mechanical Engineering Congress and Exposition, Atlanta, GA, USA, 1996.

[33] A. Gyobu, Y. Kawamura, H. Horikawa, and T. Saburi, "Martensitic transformations in sputter-deposited shape memory Ti-Ni films," presented at JIM '95 Fall Annual Meeting, Hi, USA, 1995.

[34] A. Tylikowski and R. B. Hetnarski, "Semiactive control of a shape memory alloy hybrid composite rotating shaft," *International Journal of Solids and Structures*, vol. 38, pp. 9347-57, 2001.

[35] D. Grant and V. Hayward, "Controller for a high strain shape memory alloy actuator: quenching of limit cycles," presented at 1997 IEEE International Conference on Robotics and Automation (Cat. No.97CH35992) Proceedings of International Conference on Robotics and Automation, Albuquerque, NM, USA, 1997.

[36] M. C. Piedboeuf, R. Gauvin, and M. Thomas, "Damping behaviour of shape memory alloys: strain amplitude, frequency and temperature effects," *Journal of Sound and Vibration*, vol. 214, pp. 885-901, 1998.

[37] R. Lammering and I. Schmidt, "Experimental investigations on the damping capacity of NiTi components," *Smart Materials and Structures*, vol. 10, pp. 853-9, 2001.

[38] K.-H. Ip, "Energy dissipation in shape memory alloy wires under cyclic bending," *Smart Materials and Structures*, vol. 9, pp. 653-9, 2000.

[39] C. Craciunescu and M. Wuttig, "Extraordinary damping of Ni-Ti double layer films," *Thin Solid Films*, vol. 379, pp. 173-5, 2000.

[40] K. Hishitani, M. Sasaki, D. Imai, Y. Kogo, N. Urahashi, and N. Igata, "Internal friction of TiNi alloys produced by a lamination process," *Journal of Alloys and Compounds*, vol. 333, pp. 159-64, 2002.

[41] S. Golyandin, S. Kustov, K. Sapozhnikov, M. Parlinska, R. Gotthardt, J. Van Humbeeck, and R. De Batist, "Structural anelasticity of NiTi during two-stage martensitic transformation," presented at 12th International Conference on Internal Friction and Ultrasonic Attenuation in Solids, Buenos Aires, Argentina, 1999.

[42] X. L. Liang, X. Ren, H. M. Shen, Y. N. Wang, K. Otsuka, and T. Suzuki, "Ultrasonic attenuation study of TiNi and TiNiCu single crystals," *Scripta Materialia*, vol. 45, pp. 591-6, 2001.

[43] S. Saadat, M. Noori, H. Davoodi, Z. Hou, Y. Suzuki, and A. Masuda, "Using NiTi SMA tendons for vibration control of coastal structures," *Smart Materials and Structures*, vol. 10, pp. 695-704, 2001.

[44] R. Gotthardt, P. Scherrer, and R. Stalmans, "Smart materials based on shape memory alloys: examples from Europe," presented at International Symposium and Exhibition on Shape Memory Materials (SMM '99), Kanazawa, Japan, 1999.

[45] S. P. Beyaev, E. D. Vdovin, A. E. Volkov, and A. V. Voronkov, "Experimental study and simulation of vibrations in TiNi controlled by periodic martensitic transformations," presented at Optimization and Control in Civil and Structural Engineering Proceedings of Fifth International Conference on the Application of Artificial Intelligence to Civil and Structural Engineering, Oxford, UK, 1999.

[46] S. P. Belyaev, A. E. Volkov, and A. V. Voronkov, "Mechanical oscillations in TiNi under synchronized martensite transformations," *Transactions of the ASME. Journal of Engineering Materials and Technology*, vol. 121, pp. 105-7, 1999.

[47] L. Yong, J. Van Humbeeck, R. Stalmans, and L. Delaey, "Damping related properties of NiTi shape memory alloy," presented at In Honor of Professor C.M. Wayman on the Occasion of His Retirement International Conference on Displacive Phase Transformations and their Applications in Materials Engineering. In Honor of Professor C M Wayman on the Occasion of His Retirement, Urban, IL, USA, 1996.

[48] K. Wu, S. K. Dalip, Y. Liu, and Z. Pu, "Damping characteristics of R-phase NiTi shape memory alloys," presented at Smart Materials, San Diego, CA, USA, 1995.

[49] J. Wang, X. Ma, L. Cui, F. Chen, and D. Yang, "Research on damping characteristics of NiTi shape memory alloys," *Journal of Dalian University of Technology*, vol. 36, pp. 189-92, 1996.

[50] J. van Humbeeck, J. Stoiber, L. Delaey, and R. Gotthardt, "The high damping capacity of shape memory alloys," *Zeitschrift fur Metallkunde*, vol. 86, pp. 176-83, 1995.

[51] J. van Humbeeck and Y. Liu, "Shape memory alloys as damping materials," presented at International Symposium and Exhibition on Shape Memory Materials (SMM '99), Kanazawa, Japan, 1999.

[52] Y. Liu and J. van Humbeeck, "On the damping behaviour of NiTi shape memory alloy," presented at IVth European Symposium on Martensitic Transformations, ESOMAT '97, Enschede, Netherlands, 1997.

[53] J. D. Busch, A. D. Johnson, C. H. Lee, and D. A. Stevenson, "Shape-memory properties in Ni-Ti sputter-deposited film," *Journal of Applied Physics*, vol. 68, pp. 6224-6228, 1990.

[54] Y. Kawamura, A. Gyobu, H. Horikawa, and T. Saburi, "Martenistic transformations and shape memory effect in Ti-Ni sputter-deposited thin films," presented at Icomat 95, Lausanne, Switzerland, 1995.

[55] A. Gyobu, Y. Kawamura, T. Saburi, and M. Asai, "Two-way shape memory effect of sputter-deposited Ti-rich Ti-Ni alloy films," *Materials Science & Engineering A (Structural Materials: Properties, Microstructure and Processing)*, vol. A312, pp. 227-31, 2001.

[56] D. S. Grummon, J. Zhang, and T. J. Pence, "Relaxation and recovery of extrinsic stress in sputtered titanium-nickel thin films on (100)-Si," presented at International Conference on Martensitic Transformations, San Carlos de Bariloche, Argentina, 1998.

[57] I. W. Hunter, S. Lafontaine, J. M. Hollerbach, and P. J. Hunter, "Fast reversible NiTi fibers for use in microrobotics," presented at IEEE Micro Electro Mechanical Systems. An Investigation of Micro Structures, Sensors, Actuators, Machines and Robots (Cat. No.91CH2957-9), Nara, Japan, 1991.

[58] A. Ishida, M. Sato, A. Takei, Y. Kase, and S. Miyazaki, "Effect of heat treatment on shape memory behavior of Ti-Ni thin films," presented at Icomat 95, Lausanne, Switzerland, 1995.

[59] A. Ishida, M. Sato, A. Takei, and S. Miyazaki, "Effect of heat treatment on shape memory behavior of Ti-rich Ti-Ni thin films," *Materials Transactions, JIM*, vol. 36, pp. 1349-55, 1995.

[60] K. R. C. Gisser, J. D. Busch, A. D. Johnson, and A. B. Ellis, "Oriented nickel-titanium shape memory alloy films prepared by annealing during deposition," *Applied Physics Letters*, vol. 61, pp. 1632-4, 1992.

[61] A. Ishida, A. Takei, and S. Miyazaki, "Shape memory thin film of Ti-Ni formed by sputtering," presented at 12th International Vacuum Congress, The Hague, Netherlands, 1992.

[62] E. Quandt, C. Halene, A. Holleck, K. Feit, M. Kohl, and P. Schlossmacher, "Sputter deposition of TiNi and TiNiPd films displaying the two way shape memory effect," presented at Digest of Technical Papers (IEEE Cat. No.95TH8173) Proceedings of the International Solid-State Sensors and Actuators Conference - TRANSDUCERS '95, Stockholm, Sweden, 1995.

[63] S. Miyazaki and A. Ishida, "Shape memory characteristics of sputter-deposited Ti-Ni thin films," *Materials Transactions, JIM*, vol. 35, pp. 14-19, 1994.

[64] S. Kajiwara, K. Ogawa, T. Kikuchi, T. Matsunaga, and S. Miyazaki, "Unique crystallization process in sputter-deposited Ti-Ni shape memory films," presented at Ninth International Conference on Rapidly Quenched and Metastable Materials, Bratislava, Slovakia, 1996.

[65] S. Miyazaki, K. Kitamura, K. Nomura, D. Fang, and H. Tobushi, "Shape memory characteristics of Ti-Ni alloys with several specimen sizes from micrometer to millimeter," presented at Smart Structures and Materials 1996: Smart Materials Technologies and Biomimetics, San Diego, CA, USA, 1996.

[66] E. Quandt, C. Halene, H. Holleck, K. Felt, M. Kohl, P. Schlossmacher, A. Skokan, and K. D. Skrobanek, "Sputter deposition of TiNi, TiNiPd and TiPd films displaying the two-way shape-memory effect," presented at International Solid-State Sensors and Actuators Conference - TRANSDUCERS '95, Stockholm, Sweden, 1995.

[67] T. Kikuchi, K. Ogawa, S. Kajiwara, T. Matsunaga, S. Miyazaki, and Y. Tomota, "High-resolution electron microscopy studies on coherent plate precipitates and nanocrystals formed by low-temperature heat treatments of amorphous Ti-rich Ti-Ni thin films," *Philosophical Magazine A (Physics of Condensed Matter: Structure, Defects and Mechanical Properties)*, vol. 78, pp. 467-89, 1998.

[68] K. Shimomura, P. H. Shingu, and R. Ozaki, "The morphology of alpha -Fe crystals which grow in the amorphous $Fe_{80}(C_{1-x}B_x)_{20}$ alloys," *Journal of Materials Science*, vol. 15, pp. 1175-82, 1980.

[69] A. L. Greer, "Crystal Nucleation and Growth in Metallic Liquids and Glasses," presented at Acta-Scripta metallurgica Proceedings Series, New York, 1985.

[70] F. E. Luborsky, *Amorphous metallic alloys*. London; Boston: Butterworths, 1983.

[71] P. Moine, A. Naudon, J. J. Kim, A. F. Marshall, and D. A. Stevenson, "Characterization of Ni-Ti alloys synthesized by vapor quenching," presented at Third International Conference on the Structure of Non-Crystalline Materials, Grenoble, France, 1985.

[72] H. Fujita, M. Komatsu, T. Sakata, and N. Fujita, "Nucleation of crystals in amorphous materials," *Materials Transactions, JIM*, vol. 37, pp. 1350-5, 1996.

[73] K. Otsuka, T. Sawamura, and K. Shimizu, "Crystal Structure and Internal Defects of Equiatomic TiNi Martensite," *Phys. Stat. Sol.*, vol. (a) 5, pp. 457-470, 1971.

[74] L. Chang and D. S. Grummon, "Orthorhombic Martensite, Intermetallic Precipitates and Retained Austenite in Ti-Rich Ti(Ni+Cu) Sputtered Thin Films," *Materials Research Society Symposium Proceedings*, vol. 246, pp. 141-146, 1992.

[75] J. M. Phelps, "Cross-section sample preparation of a free-standing thin-film coupon for transmission electron microscopy analysis," *Microscopy and Microanalysis*, vol. 4, pp. 128-32, 1998.

[76] http://ncem.lbl.gov/frames/center.htm.

[77] M. G. Scott and P. Ramachandrarao, "The Kinetics of Crystallization of an Fe-P-C Glass," *Materials Science and Engineering*, vol. 29, pp. 137-144, 1977.

[78] A. F. Marshall, R. G. Walmsley, and D. A. Stevenson, "Crystallization of an amorphous $Cu_{88}Zr_{20}$ alloy prepared by magnetron sputter deposition," *Materials Science and Engineering*, vol. 63, pp. 215-227, 1984.

[79] Y. Makifuchi, Y. Terunuma, and M. Nagumo, "Structural relaxation in amorphous Ni-Ti alloys prepared by mechanical alloying," *Materials Science and Engineering*, vol. A226-228, pp. 312-316, 1997.

[80] R. W. Cahn and P. Haasen, *Physical metallurgy*, 3rd ed. Amsterdam; New York: North-Holland Physics Pub., Elsevier Science Pub. Co., 1983.

[81] S. Miyazaki and A. Ishida, "Martensitic transformation and shape memory behavior in sputter-deposited TiNi-base thin films," *Materials Science and Engineering*, vol. A273-275, pp. 106-133, 1999.

[82] A. Gyobu, Y. Kawamura, T. Saburi, and M. Asai, "Martensitic transformation and two-way shape memory effect of sputter-deposited Ti-rich Ti-Ni alloy films," *Journal of the Japan Institute of Metals*, vol. 64, pp. 438-43, 2000.

[83] A. Gyobu, Y. Kawamura, H. Horikawa, and T. Saburi, "Martensitic transformation and two-way shape memory effect of sputter-deposited Ni-rich Ti-Ni alloy films," presented at International Conference on Martensitic Transformations, San Carlos de Bariloche, Argentina, 1998.

[84] A. Gyobu, Y. Kawamura, T. Saburi, and H. Horikawa, "Martensitic transformation and two-way shape memory effect of sputter-deposited Ni-rich Ti-Ni alloy films," *Journal of the Japan Institute of Metals*, vol. 63, pp. 201-7, 1999.

[85] Y. Kishi, Z. Yajima, K. Shimizu, and K. Morii, "Fatigue crack growth properties and scanning electron microscopy of fatigue fracture surface of a Ti-Ni-Co shape memory alloy," presented at International Symposium and Exhibition on Shape Memory Materials (SMM '99), Kanazawa, Japan, 1999.

[86] G. Love and V. D. Scott, "Electron probe microanalysis using soft X-rays-a review. 1. Instrumentation, spectrum processing and detection sensitivity," *Journal of Microscopy*, vol. 201 pt.1, pp. 1-32, 2001.

[87] D. N. Jamieson, A. Bettiol, and C. Yang, "Focused microprobes of high energy ions-versatile analytical probes for surfaces, interfaces and devices," presented at First Vacuum and Surface Sciences Conference of Asia and Australia (VASSCAA-1), Tokyo, Japan, 1999.

[88] J. J. Friel and R. B. Mott, "Energy-dispersive spectrometry from then until now: a chronology of innovation," presented at Thirty Years of Energy-Dispersive Spectrometry in Microanalysis, Atlanta, GA, USA, 1998.

[89] E. Szilagyi, "Energy spread in ion beam analysis," presented at Fourteenth International Conference on Ion Beam Analysis/ Sixth European Conference on Accelerators in Applied Research and Technology, Dresden, Germany, 1999.

[90] C. C. Ahn, O. L. Krivanek, R. P. Burgner, M. M. Disko, and P. R. Swann, *EELS Atlas (Gatan Inc.)*, 1983.

[91] H. Luo, F. Shan, Y. Huo, and Y. Wang, "Effect of precipitates on phase transformation behavior of Ti-49 at.% Ni film," *Thin Solid Films*, vol. 339, pp. 305-8, 1999.

[92] J. Ortin and A. Planes, "Thermodynamics and hysteresis behaviour of thermoelastic martensitic transformations," presented at European Symposium on Martensitic Transformation and Shape Memory Properties, Aussois, France, 1991.

[93] A. Hedayat, J. Rechtien, and K. Mukherjee, "The effect of surface constraint on the phase transformation of Nitinol," *Journal of Materials Science*, vol. 27, pp. 5306-14, 1992.

Filename: Thesis & Paper25.doc
Directory: C:\Documents and Settings\Administrator\My
    Documents\Thesis2002
Template: C:\Documents and Settings\Administrator\Application
    Data\Microsoft\Templates\Normal.dot
Title: Effect of Devitrification Temperature on Grain Size of NiTi
    Films
Subject: Ph.D. Thesis 2002 May
Author: Michael Vestel
Keywords:
Comments: After Gronsky second read
    After Weber read
    Pictures in text
Creation Date: 5/23/2002 6:36 PM
Change Number: 4
Last Saved On: 5/23/2002 8:21 PM
Last Saved By: vestel
Total Editing Time: 70 Minutes
Last Printed On: 5/24/2002 7:30 AM
As of Last Complete Printing
    Number of Pages: 62
    Number of Words: 46,032 (approx.)
    Number of Characters: 262,384 (approx.)